

Review

Unraveling the Correlation between Structure and Lithium Ionic Migration of Metal Halide Solid-State Electrolytes via Neutron Powder Diffraction

Hao Zhang ^{1,*} , Feilong Xu ¹, Xingyu Chen ^{1,2} and Wei Xia ^{3,*} 

¹ School of Metallurgical and Ecological Engineering, University of Science and Technology Beijing, Beijing 100083, China; m202120333@xs.ustb.edu.cn (F.X.); d202110097@xs.ustb.edu.cn (X.C.)

² School of Energy and Environmental Engineering, University of Science and Technology Beijing, Beijing 100083, China

³ Eastern Institute for Advanced Study, Eastern Institute of Technology, Ningbo 315201, China

* Correspondence: haozhang@ustb.edu.cn (H.Z.); wxia@eitech.edu.cn (W.X.)

Abstract: Metal halide solid-state electrolytes (SSEs) (Li-M-X system, typically Li_3MX_6 and Li_2MX_4 , M is metal or rare-earth element, X is halogen) exhibit significant potential in all solid-state batteries (ASSB) due to wide stability windows (0.36–6.71 V vs. Li/Li⁺), excellent compatibility with cathodes, and a water-mediated facile synthesis route for large-scale fabrication. Understanding the dynamics of Li⁺ transportation and the influence of the host lattice is the prerequisite for developing advanced Metal halide SSEs. Neutron powder diffraction (NPD), as the most cutting-edge technology, could essentially reflect the nuclear density map to determine the whole crystal structure. Through NPD, the Li⁺ distribution and occupation are clearly revealed for transport pathway analysis, and the influence of the host ion lattice on Li⁺ migration could be discussed. In this review, we stress NPD utilization in metal halide SSEs systems in terms of defect chemistry, phase transition, cation/anion disorder effects, dual halogen, lattice dynamics/polarizability, and in situ analysis of phase evolution. The irreplaceable role of NPD technology in designing metal halide SSEs with enhanced properties is stressed, and a perspective on future developments of NPD in metal halide SSEs is also presented.



Citation: Zhang, H.; Xu, F.; Chen, X.; Xia, W. Unraveling the Correlation between Structure and Lithium Ionic Migration of Metal Halide Solid-State Electrolytes via Neutron Powder Diffraction. *Batteries* **2023**, *9*, 510. <https://doi.org/10.3390/batteries9100510>

Academic Editor: Atsushi Nagai

Received: 17 September 2023

Revised: 7 October 2023

Accepted: 12 October 2023

Published: 15 October 2023



Copyright: © 2023 by the authors. Licensee MDPI, Basel, Switzerland. This article is an open access article distributed under the terms and conditions of the Creative Commons Attribution (CC BY) license (<https://creativecommons.org/licenses/by/4.0/>).

Keywords: solid-state electrolytes (SSEs); metal halides; neutron powder diffraction (NPD); structure; ionic conductivity; migration behavior

1. Introduction

Rechargeable batteries have been widely applied in electric mobiles and vehicles in modern industrial society. However, conventional lithium-ion batteries (LIBs) still present safety risks originating from exploiting flammable liquid electrolytes and the lower energy density of graphite anodes than Li metal anodes [1]. It is therefore proposed that all solid-state batteries (ASSBs) which are assembled with a solid-state electrolyte (SSE) and a Li metal anode (or anode-less design [2]) could be an alternative solution to the above issues [3]. However, realizing the above vision relies on two key factors: that is, a promising high-Li⁺ ionic conductivity, and a wide enough electrochemical stability window. To fulfill these requirements, a wide range of SSEs have been developed [4–8]. One of the most famous SSEs are thiophosphates (sulfides) which often possess high ionic conductivities of >10 mS cm⁻¹ along with their ductile nature [9,10]. However, their low compatibility with typical 4 V cathode active materials (CAMs, typically LiCoO₂ and LiNi_{1-x-y}Co_xMn_yO₂) is problematic [11], since they would be oxidized at a low potential (2.5 V vs. Li⁺/Li) [12,13]. A coating of CAM is expected to address this problem, but searching for suitable materials with proper coating-processing to achieve a homogeneous [14] functional coating [15] is not that simple. Therefore, developing new SSEs with high-Li⁺ ionic conductivity, high stability/compatibility, and ductility is still a hot topic.

Recently developed metal halides exhibit great potential as promising SSEs [14]. Metal halides are capable of achieving wider stability windows since their anions are more electronegative than oxygen or sulfur [16,17]. In fact, metal halide SSEs were investigated decades ago, but early halides (Li_2MgCl_4 , LiAlCl_4 , etc.) [17–20] failed to attract wide interest due to relatively low- Li^+ ionic conductivity. Only until recently in 2018, when Asano et al. developed a poorly crystalline Li_3YCl_6 solid electrolyte [21] that has a relatively high ionic conductivity of 0.51 mS cm^{-1} and stable cycling in ASSBs with uncoated LiCoO_2 , did halide electrolytes spur renewed interest in this system. Today, several halides have been successfully found to simultaneously possess room-temperature high- Li^+ ionic conductivity ($>10^{-3} \text{ S cm}^{-1}$), ideal oxidative stability ($>4 \text{ V}$) and compatibility with CAMs. These include typical Li_3MX_6 -typed halides Li_3InCl_6 [22,23], $\text{Li}_{3-x}\text{M}_{1-x}\text{Zr}_x\text{Cl}_6$ ($\text{M} = \text{Y, Er, Yb}$) [24,25], $\text{Li}_x\text{ScCl}_{3+x}$ [26], $\text{Li}_{2.25}\text{Zr}_{0.75}\text{Fe}_{0.25}\text{Cl}_6$ [27], $\text{Li}_{2.60}\text{Yb}_{0.60}\text{Hf}_{0.40}\text{Cl}_6$ [28], Li_3YBr_6 [21] and spinel-typed $\text{Li}_2\text{Sc}_{2/3}\text{Cl}_4$ [29]. Others, like Li_3YCl_6 [21], Li_2ZrCl_6 [27], also exhibit good oxidative and chemical stability but a little lower (10^{-4} – 10^{-3}) ionic conductivity. $\text{Li}_3\text{Y}_{1-x}\text{In}_x\text{Cl}_6$ [30] also has a conductivity surpassing $10^{-3} \text{ S cm}^{-1}$ along with a high humidity tolerance. Up to now, most of these promising halides have been chlorides and bromides. Although fluorides possess the widest electrochemical window, their room-temperature ionic conductivity is considerably lower [31]. Generally, with obvious advantages of high ionic conductivity, good stability, humidity tolerance and facile synthesis routes, metal halide electrolytes have become increasingly attractive.

In searching for new metal halides as SSEs, neutron powder diffraction (NPD) [32] is a powerful technique since it determines the whole crystal structure, especially the Li^+ sublattice, and analyzes the Li^+ migration pathway. It offers an essential understanding of the interplay between the structure and underlying Li^+ migration mechanism. NPD data is usually collected on a diffractometer in the national neutron beam center. It has played an increasingly indispensable role in the in-depth study of SSEs. Similar to X-ray diffraction (XRD), NPD also follows the Bragg diffraction law and diffraction geometry, and its structure-determination also follows a similar mathematical procedure: that is, firstly determining the phases of the structure factors, and secondly conducting an inversed Fourier transform to yield a 3D atomic distribution map of the rough crystal structure, followed by Rietveld refinements with least-square method to yield a final structure.

One unique advantage of NPD is that a neutron can pass through an electron cloud to directly interact with a nucleus, which is in a clear contrast to XRD, that only resonates with electron clouds. Using this capability, neutron diffraction can detect nuclei-density distribution rather than electron-cloud distribution in the crystal structure, which indicates a precise determination of true atomic positions in the structure model. Another advantage of NPD resides in its superior sensitivity to light elements H(D), Li, C, N, O, etc., while XRD is much weaker in detecting them. This is because NPD has a totally different elemental scattering length/intensity compared to XRD. In XRD, scattering intensity is proportional to the atomic number. The more electrons surround it, the stronger scattering intensity the atom contributes. Therefore, XRD is excellent in detecting heavy atoms (like metals or halogens) but very insensitive to light elements. However, NPD does not follow this rule, and its elemental scattering intensity depends on the interaction between neutron and nucleus. Since the intensity/interaction of light atoms is not much weaker than heavy atoms, the light atoms can be well-distinguished from heavy atoms, especially lithium, due to its negative neutron scattering length [32]. Last but not least, unlike XRD, neutron scattering intensity does not undergo obvious decay as the diffraction angle increases. This feature guarantees its high-angular (low d -spacing) signal to be of sufficient quality for further analysis of the local Li coordination environment and disorder. Besides all of the above, one may argue that Raman spectra also involves scattering. However, a Raman incident beam cannot trigger diffraction since its wavelength is too high (NPD and XRD wavelength is usually $0.1\text{--}3 \text{ \AA}$ corresponding to interplanar spacing), which means there is no diffraction peak at a certain angle, representing certain hkl indices. Raman spectra come from inelastic scattering, while NPD or XRD peaks come from elastic scattering, which

means that Raman spectra undergo adsorption/excitation to identify components, type of bonding and functional groups via a shift in wave number. However, it is unable to locate atomic positions in a 3D crystal structure model as NPD or XRD does. In general, NPD is the only technique capable of precisely determining Li^+ nuclei locations in the lattice, along with their surrounding chemical environments and sublattice.

In this review, we will mainly discuss application of NPD in metal halide SSEs. We will discuss (i) the crystallography of metal halide systems, a fundamental understanding in Li^+ transport kinetics, and basic principles of NPD data processing in analyzing structure and migration behavior; (ii) details of NPD application in defects, phase transition, cation order-disorder, dual-halogen and lattice dynamics, new structure determination, and in situ analysis of phase evolution. Several representative works are chosen for a detailed discussion of how NPD refinements determine the Li^+ ions distribution, calculate the overall energy landscape and pathways, and clarify the structural modulation mechanism for Li transport. Taken as a whole, this review will provide an insightful perspective on future developments in NPD technology applied in advanced metal halide SSEs.

2. Fundamentals in Metal Halides and Neutron Powder Diffraction (NPD)

2.1. Crystallography

For a metal halide, its stacking structure is dependent on the arrangement of ions with a different radius and polarity. In halides, anions have larger ionic radii (Shannon radius [33], F^- 122 pm, Cl^- 167 pm, Br^- 182 pm, I^- 202 pm) than metal cations (88–118 pm) and Li^+ ions (Li^+ is 73 pm in tetrahedra, and 90 pm in octahedra). Therefore, the structural framework generally depends on an anion stacking sublattice and is modulated by the polarity and radius/volume of the cation species. According to the law of ionic packing, only when the cations and anions are in close contact (tightly stacking) can the structure be stable. Here, the radius ratio of cation to anion (r^+/r^-) is represented by δ . From a solid geometry deduction, when δ ranges from 0.732 to 1, the cation will adopt a MX_8 cubic polyhedron similar to that in CsCl structure. When δ is between 0.414 and 0.732, the smaller cation will coordinate with six anions to form an MX_6 octahedron. When the cation is even smaller, it will adopt an MX_4 tetrahedral structure with δ from 0.255 to 0.414, or an MX_3 triangle structure with δ from 0.155 to 0.255. Table 1 summarizes the Shannon radii [33] of halide cations and anions. Fluorides generally have a $\delta_{\text{M/F}}$ higher than 0.732 and therefore they prefer a LiMF_4 -typed structure with a coordination environment of an MF_8 cubic polyhedron. Other halides generally have a δ ranging from 0.414 to 0.732, forming a Li_3MX_6 -typed structure with a coordination environment of an MX_6 octahedron.

Ternary chloride Li_3MCl_6 often adopts hexagonal close-packing (hcp) or cubic close-packing (ccp) for its Cl^- sublattice structures [17]. The hcp anion lattice can be further divided into a trigonal structure (space group $P-3m1$, marked as hcp-T), and orthorhombic structure (space group $Pnma$, marked as hcp-O). The difference between hcp-O and hcp-T is that, while their Cl^- adopts ABAB stacking, their Li^+ and M^{3+} in octahedral sites obey orthorhombic and tetragonal symmetric arrangements, respectively. As for ccp, its anion Cl^- sublattice adopts an ABCABC stacking, but its cations adopt a monoclinic arrangement that makes the total structure monoclinic (marked as ccp-M). In fact, for all the above structures, it is the M metal radius that decides the lattice symmetry. When the M^{3+} Shannon radius [33] is in the range of 106.3 pm (Tb^{3+})~102 pm (Tm^{3+}), the Li_3MCl_6 lattice adopts a hcp-T structure with $\delta_{\text{M/Cl}}$ among 0.611~0.637. When M^{3+} gets smaller, that is 102 pm~100 pm (i.e., Yb^{3+} and Lu^{3+}), the Li_3MCl_6 structure will transform to the hcp-O with $\delta_{\text{M/Cl}}$ among 0.599~0.611. When the M^{3+} radius further reduces, the anion sublattice will transform from hcp to ccp, as illustrated by Li_3InCl_6 ($\delta_{\text{In/Cl}} = 0.563$) and Li_3ScCl_6 ($\delta_{\text{Sc/Cl}} = 0.530$). In contrast to the chloride-based ternary halides, bromide and iodide (Li_3MBr_6 and Li_3MI_6) all adopt the same monoclinic ccp-M structure [17].

Table 1. Polarizability, Pauling radius and Shannon radius of cations and anions in metal halide SSEs. Reproduced with permission: copyright 2021, American Chemical Society [14].

Ion	Li ⁺	In ³⁺	Sc ³⁺	Y ³⁺	Er ³⁺	La ³⁺ ~Lu ³⁺	F ⁻	Cl ⁻	Br ⁻	I ⁻
polarizability α , (Å ³)	0.03	0.51	0.286	0.55	0.69	~1.14–0.606	1.04	3.66	4.77	7.10
Pauling radius (pm)	76	80	74.5	90	89	~103.2–86.1	136	181	195	216
Shannon radius ^a (pm)	90	94	88.5	104	103	~117.2–100.1	122	167	181	202
$\delta_{M/F}$	0.74	0.77	0.73	0.85	0.84	~0.96–0.82				
$\delta_{M/Cl}$	0.54	0.56	0.53	0.62	0.62	~0.62–0.60				
$\delta_{M/Br}$	0.50	0.52	0.49	0.57	0.57	~0.57–0.55				
$\delta_{M/I}$	0.45	0.47	0.44	0.51	0.51	~0.51–0.50				

^a the data comes from Shannon's work [33].

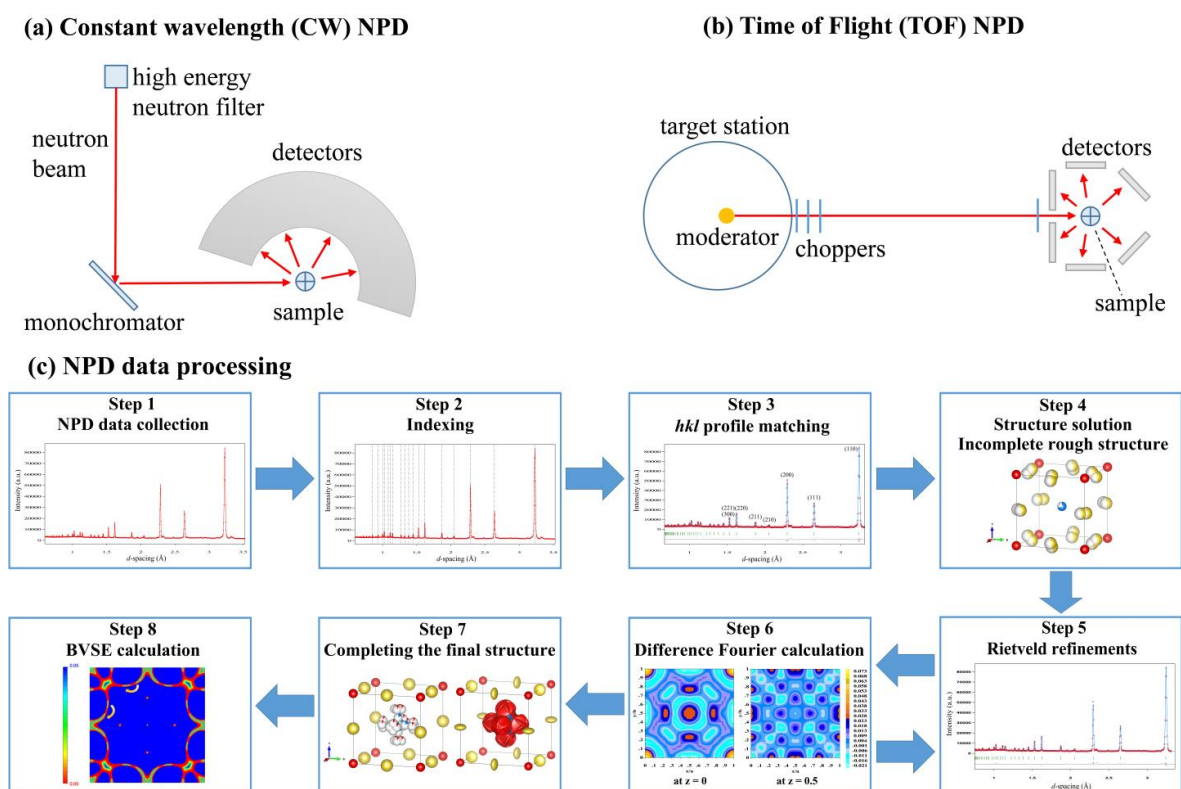
2.2. Li⁺ Migration Kinetics

The Li⁺ ions' transport behavior is strongly dependent on the crystal lattice. In a monoclinic ccp-M structure [16,21], Li⁺ ions migrate along shared-edge octahedral sites which are connected by tetrahedral interstitial sites that form a 3D isotropic diffusion network. In a structure with hcp anion arrangements (hcp-O and hcp-T) [16], Li⁺ ions transport in a similar way via octahedra and interstitial tetrahedra in the ab-plane, but only via octahedra along the c-axis, since neighboring octahedral sites are directly linked to form the diffusion paths. It worth mentioning that, in contrast to a long-range order crystal lattice, local order–disorder of the Li⁺ sublattice can exist as a unique feature in a halide lattice, which is often accompanied by local octahedra distortion and phase transition due to defects. Both the disorder and distortion significantly affect the Li⁺ migration behavior. In addition, Li⁺ transport kinetics can be modulated by polarity-induced lattice dynamics. The proximity of metal ions will also stimulate or block the Li⁺ hopping (blocking effects), which influences Li⁺ transport kinetics.

2.3. NPD Data Processing

Similar to XRD, NPD also follows the Bragg diffraction law and diffraction geometry. As shown in Scheme 1a,b, NPD can be performed using a constant wavelength (CW) neutron beam or time-of-flight (TOF) neutron beam. The NPD data can be processed by Jana [34], Fullprof [35], etc. Conventionally, as shown in Scheme 1c, NPD data-processing includes the following steps: (1) Data collection. Instrument scientists will help users to load a powder sample in the sample holder on the diffractometer. A neutron beam will penetrate the sample and trigger diffraction. Multiple detectors at different angles will simultaneously collect diffraction peaks. After data correction, the original NPD data is returned to the users. (2) Indexing. If the crystal structure is already known, then this step can be skipped. However, if the structure is new (unknown, unreported), then this step is unavoidable. One needs to identify most diffraction peaks and then run an "indexing" function to find out the lattice type, lattice parameters, and space group. Note that indexing can be pre-run in the XRD pattern. The indexed lattice must be in agreement with TEM diffraction. (3) *hkl* Profile matching. This is also a refinement procedure. Before solving the atomic positions, one needs firstly to refine the peak shape, peak asymmetry (if it has any), zero shift, background and lattice parameters, with correct instrument parameters. Each peak and the background line should be well-simulated, usually with a total evaluating factor $\chi^2 < 2$. Since the program will later extract these simulated peak intensities of *hkl* indices for structure solution and structure refinements, this profile-matching step must be well-done. (4) Structure solution. If the structure model is already known, then this step is skipped. If it is new, then one must run a "solve" function. The program will try to solve the phases of structure factors and finally return a rough structure model via an inversed Fourier transform. This rough model is usually incomplete, and may have some flaws or mistakes in atom positions. (5) Rietveld refinements with structure model. By the least-square method, parameters like atom positions, occupancies and thermal displacements

will be refined. As the simulated intensities (of the structure model) gradually approach the observed ones, the structure model is getting more and more close to the true crystal structure. (6) Difference Fourier calculation. This is to check the residue nuclei densities in the structure and to identify if they represent missing atoms. One needs to complement the missing atoms in the structure model and go back to step (5) to refine again, until all of the atoms are found out. (7) Completing the structure. After locating all the atoms, final rounds of refinements are needed to complete the whole structure. The structure and all parameters should be chemically reasonable, and evaluating factors should be within an acceptable range, empirically, $\chi^2 < 2$, $R_{wp} < 13\%$. (8) Bond-valence site energy (BVSE) calculation [36,37]. On the basis of this refined structure and hkl intensities, the BVSE will calculate the overall landscape of Li^+ site energy and point out possible Li^+ diffusion pathways in the structure.



Scheme 1. (a) A schematic layout of constant wavelength (CW) NPD technique. It follows the same diffraction law and geometry as XRD. However, a circular array of multiple detectors will together rotate and collect diffraction peaks in different bands at the same time. (b) A schematic layout of time-of-flight (TOF) NPD technique. Detectors are fixed at certain angles, collecting diffraction peaks in different wavelength. The wavelength can be calculated according to neutron flying time. Then, the diffraction peaks can be nominated to different d values. (c) NPD data processing. Here we use our published work on sodium SSEs Na_3ONO_2 for illustration. One can see how we proceed with our TOF data to finally ascertain the structure. For the NPD data in step 1, 2, 3, and 5, red dots represent observed data. Blue line represents simulated data. Green bars are indices. Gray line at bottom represents difference between observed and simulated data. In step 4 and 7, the red sphere is O^{2-} , the yellow sphere is Na^+ , the blue sphere is N^{3+} . In step 7, note that one cell has one NO_2^- , but NO_2^- is located around the body center with disordered orientation, so its occupancy on each site is very low (left structure). The anisotropic thermal displacements of Na^+ and NO_2^- are also obtained (right structure). Step 6 shows the residue nuclei densities (%) at $z = 0$ and $z = 0.5$ cross sections. In step 8, a cross section at $z = 0$ shows a possible Na^+ migration pathway (yellow arrow). Reproduced with permission: Copyright 2020, Royal Society of Chemistry [38].

For halide SSEs, NPD data can be singly used in a structure solution and subsequent Rietveld refinement to identify the Li^+ distribution, which provides critical evidence to elucidate the mechanism of Li^+ transport enhancement. In situ NPD as heating or charging/discharging can be used to monitor the dynamic process of continuous phase/structure evolution. Besides the above single usage, NPD and XRD/Synchrotron are often jointly refined to tackle a complicated structure or new structural phase. In this joint-refinement, NPD and XRD will be simultaneously refined. The XRD/Synchrotron data use their good advantage in detecting heavy ions (Cl^- , Br^- , Y^{3+} , In^{3+} , Zr^{4+} , etc.) to quickly settle the whole lattice framework, while NPD data focus on locating Li^+ ions and quantifying their chemical occupancy.

Whether singly or jointly used, the first important step is always to check the lattice type (space group) and lattice parameters, which give preliminary information on phase transition and lattice evolution. Note that lattice evolution is often associated with a distortion or tilting of Li/metal octahedra, which essentially affects Li^+ migration behavior. The second step is to analyze the position (coordinates), occupancy, and isotropic/anisotropic thermal displacement of all ions. These three factors provide key information on the following: Li^+ order–disorder, the existence of new Li sites, vacant interstitial sites (as intermediate states for ionic motion), blocking effects from metal ions, distortion or tilting of Li/Metal octahedra, dual-halogen mixing, etc. Particularly, Li^+ thermal displacements are associated with migration behavior and anion lattice modulation. Last but not least is the difference Fourier procedure, which is based on the difference between simulated and observed hkl intensities to calculate residual nuclei densities in one's structure model. Some of these residual densities may represent missing atoms. Difference Fourier procedure is significantly advantageous in discovering unexpected new Li^+ sites which may reside in Li^+ migration pathways and promote the migration.

The comprehensive structure model determined by neutron powder diffraction refinements enable the probable Li^+ migration pathways to be revealed via a bond-valence site energy (BVSE) calculation [36,37]. Li^+ site energies, $E_{\text{BVSE}}(\text{Li})$, will be calculated and presented in the form of a dense grid of points throughout the whole structure with the user-defined resolution (for instance 0.1 Å) using the Morse-type SoftBV interaction potential. An overall 3D isosurface landscape of $E_{\text{BVSE}}(\text{Li})$ will be depicted, superimposed upon the crystal structure. Regions of low BVSE can be identified as probable Li^+ diffusion pathways. Metastable interstitial Li^+ sites as a possible transition state for motion in the pathway can even be found. Moreover, an energy profile along certain migration pathways can be extracted from the above overall landscape to further analyze the migration barrier. The above information provides an intuitive explanation as to how structural modulation exactly affects migration behavior.

3. Application of Neutron Powder Diffraction (NPD) in Metal Halides SSEs

3.1. Defect Chemistry and Phase Transition

Defects in the solid-state structure, which are often accompanied by phase transition and local structure distortion, directly affect active Li^+ and vacancy concentrations. Since the Li^+ hopping process is very sensitive to these concentrations, tuning defects can be an effective strategy towards a facile Li^+ hopping process, which in turn boosts the ionic conductivity in orders of magnitude. The ion transport via vacancies is the predominant migration behavior for many kinds of superionic conductors [39]. According to one study [39], in the close-packed lattice, the Li^+ migration barrier through vacancies is much lower than the direct or ring exchange diffusion process. In a layered structure, the Li^+ ion would prefer to migrate from one octahedron site to another via their adjacent tetrahedral vacancy. For layered Li_3MX_6 -type halides, when the compound is stoichiometric, there are 1/3 vacancies that reside in octahedral interstitial sites. These vacancies are essential in achieving high ionic conductivity in the Li_3MX_6 structure.

An aliovalent substitution of metal ions could readily enrich the active Li^+ and vacancy concentration to improve the ionic conductivity. The increased vacancy concentration may

lead to a redistribution of Li ions, and even bring new Li⁺ sites (as new active Li⁺). It also should be noted that aliovalent substitution often triggers phase transition and distortion in the lattice. Here we discuss four published works [24,40–42] to show how NPD assists the above study.

The first work is about a Zr⁴⁺ substituted halide system Li_{3-x}M_{1-x}Zr_xCl₆ (M = Y, Er) ($x = 0-0.6$) that mainly involves the finding of a new Li⁺ site after phase transition, as reported by Park et al. [24]. Zr⁴⁺ ($r = 72$ pm) was specifically adopted to substitute Y³⁺ ($r = 90$ pm) and Er³⁺ ($r = 89$ pm) since its ionic radius is larger than other M⁴⁺ metal ions. After substitution, the halide transits from a trigonal to an orthorhombic structure, and achieves a highest room-temperature ionic conductivity of 1.1×10^{-3} S cm⁻¹ at $x = 0.367$ for Li_{3-x}Er_{1-x}Zr_xCl₆ (phase III, orthorhombic *Pnma*), and 1.4×10^{-3} S cm⁻¹ at $x = 0.5$ for Li_{3-x}Y_{1-x}Zr_xCl₆ (phase III, orthorhombic *Pnma*). Such ionic conductivity is among the top class of reported chloride compounds. The author also discovered that orthorhombic Li_{3-x}M_{1-x}Zr_xCl₆ has excellent electrochemical oxidation stability against non-coated 4 V-class cathode materials that does not show any observable oxidative interfacial decomposition in full cells. It was concluded that the phase transition from trigonal to orthorhombic structure and additional Li⁺ sites (marked as Li3) account for the superior conductivity.

TOF NPD was performed in combination with single crystal XRD. First, they used single-crystal XRD to solve the location of heavy ions Er³⁺, Y³⁺, Zr⁴⁺, Cl⁻. Second, this model was directly used in neutron diffraction Rietveld refinements to refine the Li⁺ position (while keeping the heavy ions fixed). Third, the Er/Zr ratio was set to the single-crystal value while other parameters like occupancies and thermal displacements were freely refined. Note that a constraint on total Li occupancy was added for charge balance. The final NPD refinement plot is shown in Figure 1a, which is often presented in research papers including observed neutron data, a mathematically calculated line obtained from the final structure, index of diffraction peaks (indicating which plane the peak belongs to), and difference between observed and calculated data. Empirically, when the χ^2 (=GoF²) is lower than 2, along with a residual factor R_{wp} lower than 13%, the refinement result is acceptable.

The trigonal-to-orthorhombic phase transition as identified by NPD data is shown in Figure 1b. Pristine Li₃ErCl₆ and Li₃YCl₆ are trigonal in structure (space group *P-3m1*, marked as phase I). When Zr⁴⁺ is $0.2 \leq x \leq 0.3$, the phase transition occurs and an orthorhombic Li₃LuCl₆-typed [43] structure (*Pnma*, phase II) appears. At higher substitution levels ($0.367 \leq x \leq 0.600$), the MCl₆ octahedra undergo further tilting that distorts the orthorhombic structure (*Pnma*, phase III). Tilting or distortion of octahedra often happen with phase transition.

The new tetrahedral Li3 site that is about 20% occupied was only observed in phase III, as shown in Figure 1c,d. In phase III, the Li1 and Li2 octahedra are face-shared in pairs, and the Li3 tetrahedron connects these Li1/Li2 octahedral pairs in a trigonal face-shared manner to establish Li⁺ ion diffusion chains along the *a*-axis. Note that all three Li⁺ sites contain a significant vacancy population between 25% and 80%. The emergence of a Li3 tetrahedral site indicates a redistribution of Li⁺ ions. As concluded by the author, these Li3 sites and vacancies are responsible for the higher Li⁺ conductivity in phase III.

Bond-valence site energy (BVSE) methods [36,37] can calculate the energy landscape of the Li⁺ diffusion pathway. In Figure 1e, the [Li3–Oct.–Li3–Li2] zigzag chain running along the [010] direction was the most desired one-dimensional pathway. This pathway along the *b*-axis intersects with [Li2–Li3–Li1] chains of the *ac*-plane (Figure 1f) to form a 3D network for Li⁺ migration. In Figure 1g, a metastable octahedral interstitial site, namely “Oct”, which is face-shared with Er/Zr octahedra, was suggested to participate in the Li⁺ migration. Moreover, the site energy profile (Figure 1h) extracted from the overall landscape reveals a lower energy barrier for orthorhombic Li_{2.5}Er_{0.5}Zr_{0.5}Cl₆ (phase III). The barrier for trigonal Li₃ErCl₆ (phase I) was claimed to be about 1.5-fold higher than this orthorhombic one.

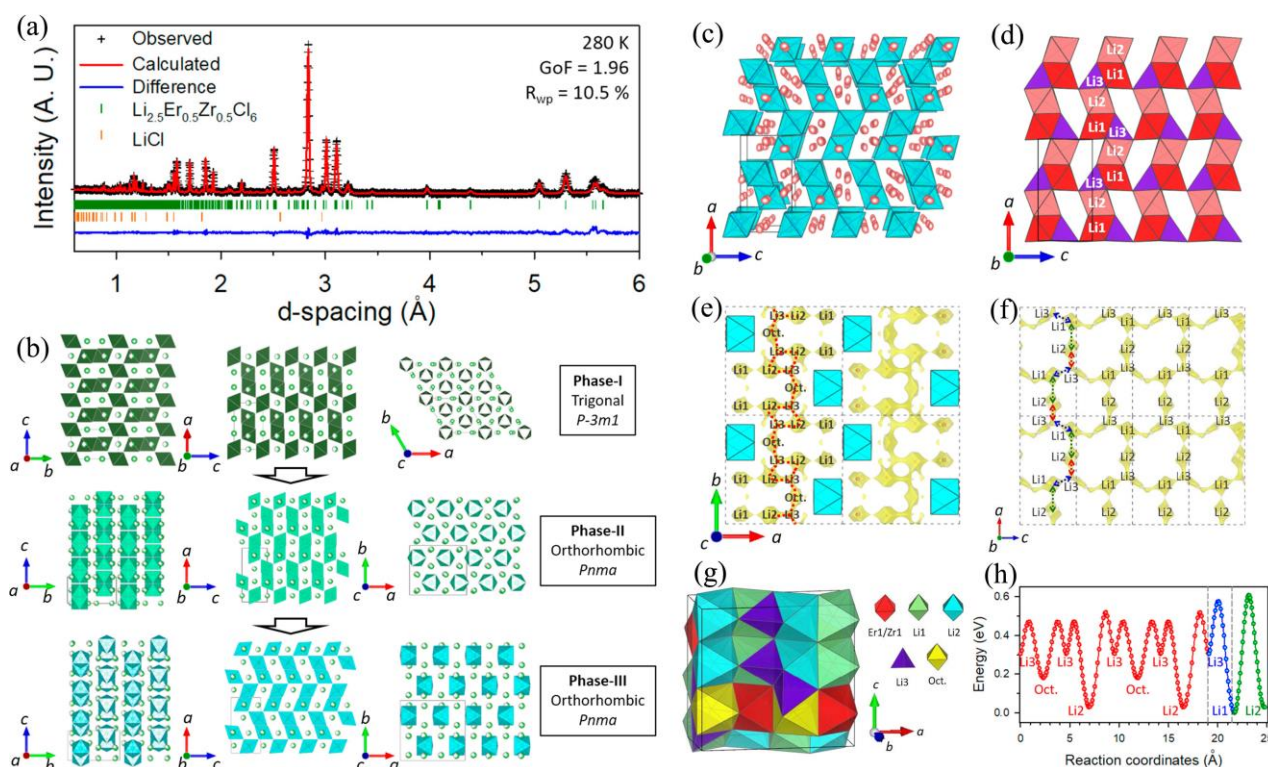


Figure 1. (a) TOF NPD data of $\text{Li}_{2.5}\text{Er}_{0.5}\text{Zr}_{0.5}\text{Cl}_6$ at 280 K and its Rietveld refinement. Black crosses represent experimental data; the red line is the simulated pattern; the blue line is the difference; green bars represent index of Bragg reflections for $\text{Li}_{2.5}\text{Er}_{0.5}\text{Zr}_{0.5}\text{Cl}_6$ with ratio of 99.24%, and orange bars for impurity LiCl with ratio of 0.76%. (b) Phase evolution of $\text{Li}_3\text{M}_{1-x}\text{Zr}_x\text{Cl}_6$ ($\text{M} = \text{Er}, \text{Y}$) upon Zr substitution. (c) View along $[010]$ direction of the b -axis in $\text{Li}_{2.5}\text{Er}_{0.5}\text{Zr}_{0.5}\text{Cl}_6$. Blue polyhedrals represent Er1/Zr1 octahedra, red spheres represent Li ions. (d) View along $[010]$ direction showing the connectivity of Li1/Li2 octahedra pairs and Li3 tetrahedra. (e,f) 1D migration pathway (red dots) viewed along different direction. Yellow isosurface represents constant $E_{\text{BVSE}(\text{Li})}$. (g) Slice of the structure showing octahedra and tetrahedra including “Oct”. (h) Site energies landscape obtained from BVSE [36,37]. Li1 sites are set to zero since they are of the lowest energy. The red portion represents the Li migration pathway of lowest energy as marked by red dots in (e). The blue and green portions represent overall 2D and 3D migration energies, respectively. Reproduced with permission: Copyright 2020, American Chemical Society [24].

The second work is about $\text{Li}_{3-x}\text{In}_{1-x}\text{Zr}_x\text{Cl}_6$ [40] that mainly involves octahedral distortion, accompanied with Li^+ redistribution and Li^+ -metal cations disorder (disorder will be discussed further in a following section). The author concluded that local M2/Li4 octahedra distortion, along with Li^+ redistribution and disorder, accounts for the conductivity improvement from $0.47 \text{ mS}\cdot\text{cm}^{-1}$ of Li_3InCl_6 to $1.25 \text{ mS}\cdot\text{cm}^{-1}$ of $\text{Li}_{2.6}\text{In}_{0.6}\text{Zr}_{0.4}\text{Cl}_6$. It should be noted that pristine Li_3InCl_6 has been reported to possess higher conductivity ($\sim 1.49 \text{ mS}\cdot\text{cm}^{-1}$ [22], $\sim 2 \text{ mS}\cdot\text{cm}^{-1}$ [23,44]) than in this work. However, this should be related to the synthesis method. It can be expected that after optimization on a synthesis route, $\text{Li}_{2.6}\text{In}_{0.6}\text{Zr}_{0.4}\text{Cl}_6$ would achieve higher conductivity than Li_3InCl_6 of $1.49\sim 2 \text{ mS}\cdot\text{cm}^{-1}$.

The indication of the existence of octahedral distortion is the lattice compression along the c -axis. The NPD refinements on the $\text{Li}_{3-x}\text{In}_{1-x}\text{Zr}_x\text{Cl}_6$ series as shown in Figure 2a,b reveal that, as Zr increases, lattice parameters a and b are nearly unchanged, while c decreases, possibly due to the smaller ionic radius of Zr^{4+} than In^{3+} ions [33]. This represents a compression on the c direction and lattice volume asymmetric shrinkage, which would act on Li /metal octahedra to undergo asymmetric distortion.

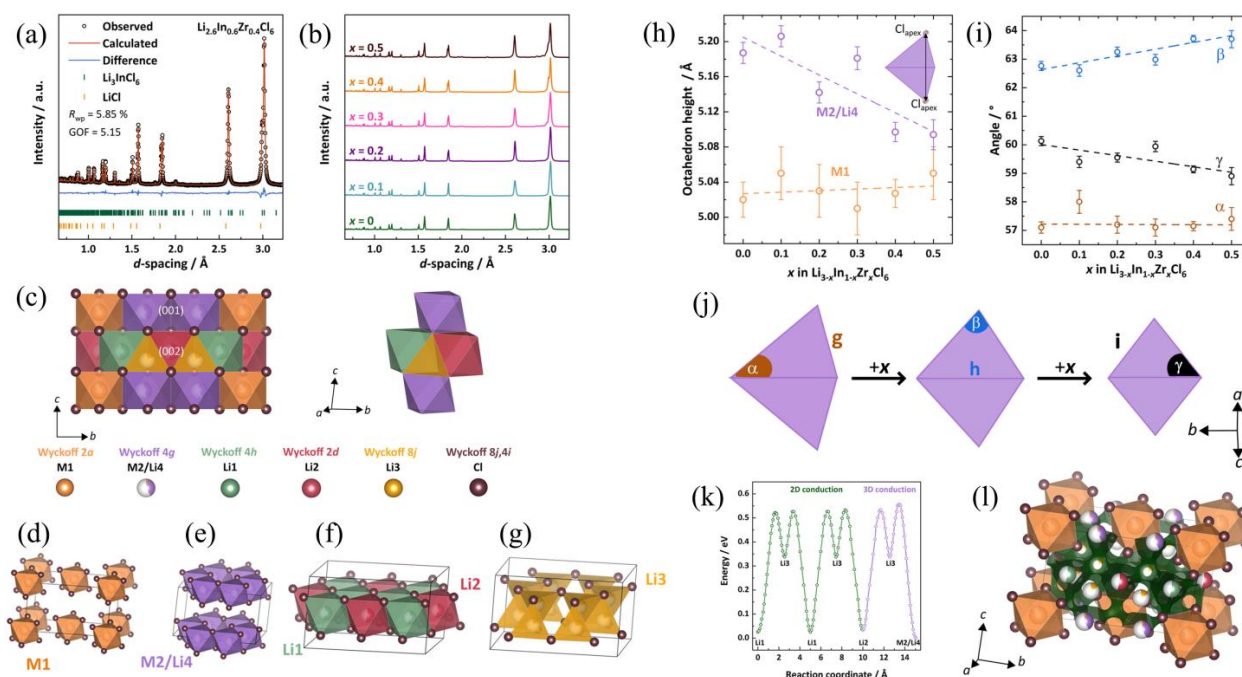


Figure 2. (a) Rietveld refinement on room-temperature NPD data of $\text{Li}_{2.6}\text{In}_{0.6}\text{Zr}_{0.4}\text{Cl}_6$. (b) Display of all $\text{Li}_{3-x}\text{In}_{1-x}\text{Zr}_x\text{Cl}_6$ ($0 \leq x \leq 0.5$) neutron diffractograms. (c) Li_3InCl_6 structure. M1 and M2 represent $[\text{InCl}_6]$ octahedra. Li1 and Li2 represent $[\text{LiCl}_6]$ octahedra. Li3 is an interstitial $[\text{LiCl}_4]$ tetrahedron. Li4 co-occupies with the M2 octahedron. Right panel is the cut out of the Li substructure showing their connectivity and framework. (d–g) Metal and lithium polyhedra on different crystallographic sites. (h) Evolution of M1 and M2/Li4 octahedra height depending on Zr^{4+} substitution. The octahedron height is indicated by the distance between two apexed Cl^- . (i) Evolution of triangular face angle on the dependence of Zr^{4+} substitution. (j) Conceptual description of M2/Li4 octahedra distortion. The distortion is exaggerated. Upon Zr^{4+} substitution, the distortion of the M2/Li4 octahedron varies according to the shift of the apical chlorides. (k) Energy landscape of preferred Li^+ diffusion pathway, in which Li3 sites are the mentioned intermediate higher energy state for the jumps among Li octahedra. (l) Isosurface of Li^+ ions, which shows possible trajectories for Li^+ diffusion, displayed in green. Reproduced with permission: Copyright 2021, American Chemical Society [40].

However, to further understand this distortion from atomic scale, structure determination based on NPD is very necessary. The crystallography is shown in Figure 2c–g. The substituted $\text{Li}_{3-x}\text{In}_{1-x}\text{Zr}_x\text{Cl}_6$ is isostructural to Li_3InCl_6 . For a typical Li_3InCl_6 , it adopts a monoclinic layered structure with space group $C2/m$. The $(\text{InCl}_6)^{3-}$ octahedra are exclusively located within the (001) lattice plane (marked as M1 and M2/Li4 in Figure 2d,e). In this (001) plane, most In^{3+} ions occupy M1 isolated octahedral sites, while only a few of them occupy M2 honeycomb sites (occupancy 5–10%). Li^+ ions only occupy M2 sites (occupancy ~40%) to make M2/Li4 co-occupation (Figure 2e). In the (002) plane, only $(\text{LiCl}_6)^{5-}$ octahedra and $(\text{LiCl}_4)^{3-}$ tetrahedra (occupancy ~17%) reside in this layer (marked as Li1, Li2, and Li3 in Figure 2f,g).

The most intriguing factor with structure is that, with Zr^{4+} substitution, In^{3+} and Zr^{4+} still prefer M1 positions with a few on the M2/Li4 position, while Li^+ ions would remarkably occupy a M2/Li4 position, together with a gradually decrease of occupancy on Li1, Li2 octahedral sites, and a total loss of occupancy on Li3 tetrahedral sites. The Li3 tetrahedral site is explained to be a higher-energy intermediate site [16] that would be depopulated first when removing Li^+ from the system. (For charge balance, Li^+ will be removed as Zr^{4+} increases.) These results represent a redistribution of Li^+ ions and a

Li-In-Zr disorder on the M2/Li4 position, which may lead to a 3D diffusion pathway for facile Li⁺ migration.

Bearing the above in mind, octahedral distortion can be discussed and its correlation with the Li sublattice can be unraveled. With Zr⁴⁺ substitution, the octahedron height of the M2/Li4 site significantly decreases (Figure 2h), while the M1 octahedron height keeps almost constant. These changes are the main reason for the *c*-direction compression. In addition, the apex Cl⁻ approaches the center, accompanied by angle changes (Figure 2i) that alter the degree of octahedral distortion (Figure 2j). Since M2/Li4 sites are preferably occupied by Li⁺ with Zr⁴⁺ substitution, the primary driven force for this distortion should be lithium redistribution and disorder. Finally, BVSE [36,37] based on neutron data provides the 3D migration pathway (Figure 2l) with its site energy profile (Figure 2k).

The third [42] and fourth [41] works are both about rare-earth metal halides that mainly involve phase transition. It has been known that Li₃MCl₆ (M = Ln³⁺) can crystallize in a trigonal (space group *P*-3*m*1), orthorhombic (space group *Pnma*) and monoclinic (space group *C2/m*) structure. Different symmetric arrangements of cations and vacancies lead to a distinct Li⁺ migration. Conventionally, Li₃MCl₆ (M = Tb, Dy, Ho, Er, Tm) crystallizes in a trigonal *P*-3*m*1 structure. However, Liang et al. [42] modified the Li/M ratio to induce a phase transition from trigonal to orthorhombic structure and successfully achieved a series of orthorhombic Li_{3-3x}M_{1+x}Cl₆ (-0.14 < *x* ≤ 0.5, M = Dy, Ho, Y, Er, Tm) with enhanced ionic conductivity. Taking orthorhombic Li_{3-3x}Ho_{1+x}Cl₆ (0.04 < *x* ≤ 0.2) as an instance, a tiny modification of the Li/Ho ratio (*x* = 0.09) could boost the room-temperature ionic conductivity from 2.9 × 10⁻⁴ S cm⁻¹ to 1.3 × 10⁻³ S cm⁻¹. NPD refinement clearly confirmed the rearrangement of the cation and anion sublattice after phase transition, and an expansion in the triangular area of face-shared octahedra/tetrahedral. It is explained that such an expansion broadens the size of the bottleneck for a facile Li⁺ diffusion along the *c*-lattice direction. The diffusion in the *c* direction via face-sharing octahedral is faster than that in the *xy*-plane via a face-sharing octa-tetra-octahedra path. Its activation energy is also reduced compared to that in the trigonal phase.

The above study can be seen as a typical example of isovalent self-substitution, in which its own rare-earth content was tuned to trigger Li vacancies and phase transition. Their success with orthorhombic Li_{2.73}Ho_{1.09}Cl₆ encouraged Zhou et al. [41] to perform aliovalent substitution on the Li_{3-x}Zr_xHo_{1-x}Cl₆ and Li_{3-x}Zr_xLu_{1-x}Cl₆ series. Zr substitution is also beneficial in relieving the dependence on rare-earth elements and promoting scalable production. In their work, Zr⁴⁺ substitution lifts the ionic conductivities up to ~1.8 mS cm⁻¹, and suppresses the activation energies down to ~0.34 eV. At cutoff potentials of both 4.3 and 4.6 V vs. Li⁺/Li, their ASSB, comprised of Li_{2.6}Zr_{0.4}(Ho/Lu)_{0.6}Cl₆ SSE paired with LiNi_{0.85}Co_{0.1}Mn_{0.05}O₂ (NCM85), show stable cycling. Even upon 4.8 V, their ASSB still exhibits long-term stable cycling. When assembled with an Si or Li_{0.7}Si anode, NCM85 ASSBs with Li_{2.6}Zr_{0.4}Lu_{0.6}Cl₆ as the SSE still perform long-term stable cycling at a high areal capacity of 16 mAh cm⁻².

Pure Li₃HoCl₆ has a trigonal structure. Similar to the above mentioned Li_{2.73}Ho_{1.09}Cl₆ and Li_{3-x}Zr_x(Y/Er)_{1-x}Cl₆ [24], the Zr⁴⁺ substituted Li_{3-x}Zr_xHo_{1-x}Cl₆ (0.2 < *x* ≤ 0.8) series transform from a trigonal to an orthorhombic-II structure (space group *Pnma*). Li₃LuCl₆ itself is an orthorhombic-I structure (space group *Pnma*), but Li_{3-x}Zr_xLu_{1-x}Cl₆ (0.2 ≤ *x* ≤ 0.8) also transform to the orthorhombic-II structure with (Lu/Zr)Cl₆ octahedra tilting. All solid solutions Li_{3-x}Zr_x(Ho/Lu)_{1-x}Cl₆ (0.2 ≤ *x* ≤ 0.6) exhibit superior conductivities (up to 1.8 mS cm⁻¹) compared to pristine Li₃HoCl₆ and Li₃LuCl₆ (~0.1 mS cm⁻¹).

NPD plays a key role in Li_{3-x}Zr_x(Ho/Lu)_{1-x}Cl₆ structure phase transition analysis and Li occupancy. In layers of the *ab*-plane, trigonal Li₃HoCl₆ and orthorhombic-I Li₃LuCl₆ both possess honeycomb-ordered shared-edge Li⁺ octahedra adjacent with their interstitial tetrahedral voids, which allow Li⁺ ions to diffuse in the *ab*-plane via the Oct-Tet-Oct pathway. Along the *c* axis, the LiCl₆ octahedra are directly linked in a face-shared manner to establish a *c*-direction Li⁺ pathway. Similar to the above, substituted orthorhombic-II Li_{2.4}Zr_{0.6}(Lu/Ho)_{0.4}Cl₆ still maintains a honeycomb ordered layer but arranged on the *bc*-

plane. These layers have a stacking fault along the *a*-axis that forms a zigzag chain of faced-shared or edge-shared LiCl_6 octahedra along the *a*-axis, which allows Li^+ migration along this direction. All of these Li sites in the above structures are not fully occupied, leaving abundant Li vacancies in the diffusion pathway, as confirmed by BVSE calculation [36,37] based on NPD. From NPD refinements, $\text{Li}_{2.4}\text{Zr}_{0.6}(\text{Lu}/\text{Ho})_{0.4}\text{Cl}_6$ possesses prominently more vacancies in its Li octahedral sites in honeycomb layers and zigzag chains compared to Li_3HoCl_6 and Li_3LuCl_6 . This is the explanation for its higher conductivity triggered by phase transition.

3.2. Disorder and Blocking Effect

The disorder discussed here refers to Li^+ disorder and metal cation disorder. Both of these are accompanied with vacancies. As we know, disorder is very common in solid structures, and also in metal halide SSEs. Even within the same anion sublattice, there could there be a remarkable difference in the disorder, according to the different type of cations. Since the structure provided by neutron/XRD refinements is actually a space-and-time-averaged one, the most common instance we can find of so-called disorder is the multiple crystallographic sites for Li^+ and cations with different partial occupancies. The common way to induce disorder is to vary the components or valence of metal cations. The induced disorder will in turn promote the Li^+ hopping in its pathway. The blocking effect means that the M cation on its position will yield a Coulombic repulsion to Li^+ migration. Therefore, the Li^+ diffusion via the interstitial tetrahedral site surrounding the M cation is to some extent blocked. Tuning or decreasing the M contents to relieve the blocking effect is plausible for better ionic conductivity.

Utilizing disorder strategies, Zhou et al. [29] construct a Li^+ and cation disordered halo-spinel chloride $\text{Li}_2\text{Sc}_{2/3}\text{Cl}_4$ with superionic conductivity as high as 1.5 mS cm^{-1} that has far surpassed other spinel-type halides Li_2MgCl_4 , Li_2ZnCl_4 ($<10^{-3} \text{ mS cm}^{-1}$ at room temperature) [45,46], and most halides including Li_3InCl_6 , Li_3YCl_6 , Li_3ErCl_6 , and $\text{Li}_{3-x}\text{M}_{1-x}\text{Zr}_x\text{Cl}_6$ ($\text{M} = \text{Er}, \text{Y}$) ($0.31\text{--}1.49 \text{ mS cm}^{-1}$) [21,24]. Such superior ionic conductivity was ascribed to the significant Li-site disorder, which creates a redistribution of Li^+ ions that brings about new Li sites (marked as Li2 and Li3). These new interstitial Li sites serve as intermediate sites residing on the pathway that are critical for Li^+ ion diffusion.

Above explanation is actually based on time-of-flight (TOF) NPD refinements that exactly determine Li^+ distribution and occupancy on each crystallographic site. As shown in Figure 3a, the neutron pattern is well refined by the $\text{Li}_2\text{Sc}_{2/3}\text{Cl}_4$ spinel structure with cubic space group *Fd-3m*. The crystal structure of spinel $\text{Li}_2\text{Sc}_{2/3}\text{Cl}_4$ are shown in Figure 3b,c. The framework of $\text{Li}_2\text{Sc}_{2/3}\text{Cl}_4$ is somewhat similar to spinel Li_2MgCl_4 , but the atomic occupancies are quite different. $\text{Li}_2\text{Sc}_{2/3}\text{Cl}_4$ possesses four Li sites: Li2 and Li3 are newly discovered positions while Li1 and Li4 are original positions similar to Li_2MgCl_4 . The conventional spinel Li_2MgCl_4 is constituted of edge-shared Mg1 and Li2 octahedra where both Mg and Li take a half occupation, and Li1 fills the corner-sharing Li1 tetrahedra site (Li1 coordinates: $1/8, 1/8, 1/8$). However, in $\text{Li}_2\text{Sc}_{2/3}\text{Cl}_4$, its edge-shared Sc1 and Li4 octahedra have a Sc:Li4 occupation ratio of 0.311:0.689, which means that more Sc ions are substituted by Li ions. While Li1 also take the same position of tetrahedra sites (similar to Li_2MgCl_4), its new Li2 fills the edge-sharing Li2 octahedra site, and its new Li3 occupy another edge-sharing tetrahedra site.

The most striking point is that the wide spread of new Li2 and Li3 over the whole lattice links the Li1 tetrahedra, Li2 octahedra, and Li3 tetrahedra all together in series in a face-shared manner that forms an infinite pathway for Li^+ diffusion in $\text{Li}_2\text{Sc}_{2/3}\text{Cl}_4$ (Figure 3d). This new pathway plays the decisive role in the ionic conductivity enhancement. In this new pathway, the relatively low occupancies of the Li1,2,3 sites have provided abundant vacancies which would help to skip the defect formation step during Li^+ ion migration. Moreover, the Li^+ redistribution over tetrahedra and octahedra sites also indicates that the Li^+ site energies on the sites are probably similar, that is, a flat energy landscape for facile ion diffusion [47,48].

A blocking effect may reside on the Sc1/Li4 octahedra site, as reflected by NPD refinements that the thermal displacement parameter of Li4 on this octahedral site is very low. Although Sc1/Li4 octahedra also border Li3 tetrahedra in a face-shared manner, trivalent Sc^{3+} ions still sit in this octahedra site that may block Li^+ ion diffusion, as Mg^{2+} does in Li_2MgCl_4 [49]. Hence, Li^+ ions on this site appear to show small thermal displacements and low mobility. Therefore, the main diffusion pathway may not involve Sc1/Li4 octahedra sites. Overall, these new possible Li1,2,3 diffusion pathways with considerable amounts of vacancies achieve a relatively low activation energy for Li^+ hopping. In a battery test, $\text{Li}_2\text{Sc}_{2/3}\text{Cl}_4$ also shows excellent performance in a potential window up to 4.6 V due to its high oxidative stability, when assembled with uncoated LiCoO_2 (LCO), $\text{LiNi}_{0.6}\text{Mn}_{0.2}\text{Co}_{0.2}\text{O}_2$ (NCM622) and high-Ni $\text{LiNi}_{0.85}\text{Mn}_{0.1}\text{Co}_{0.05}\text{O}_2$ (NCM85) cathodes.

It would be very meaningful to induce a higher extent of disorder into $\text{Li}_2\text{Sc}_{2/3}\text{Cl}_4$ to further improve ionic conductivity, along with good stability against electrodes. Zhou et al. [50] continued their research and developed an isoivalent In^{3+} substituted $\text{Li}_2\text{In}_x\text{Sc}_{0.666-x}\text{Cl}_4$ ($0 < x < 0.666$) system as a fast Li ion conducting chloride SSE, which exhibits an improved ionic conductivity up to 2.0 mS cm^{-1} ($\text{Li}_2\text{Sc}_{2/3}\text{Cl}_4$ is 1.5 mS cm^{-1}). According to their report, incorporating only 10 wt% $\text{Li}_2\text{In}_{1/3}\text{Sc}_{1/3}\text{Cl}_4$ with cathode active material (CAM, typical 4V, LiCoO_2 , $\text{LiNi}_{1-x-y}\text{Co}_x\text{Mn}_y\text{O}_2$) [11] could form a cathode composite with a low-impedance SE/CAM interface that enables excellent electrochemical performance. All-solid-state Li batteries (ASSBs) utilizing uncoated LCO, NCM622 and NCM85 could exhibit a superior rate capability and apparently more stable long-term cycling up to 4.8 V versus Li^+/Li , compared with most advancing ASSBs. Their high-voltage, high-loading and ultra-stable solid-state cells indeed provide inspiration for the design of advancing ASSBs.

In this $\text{Li}_2\text{In}_x\text{Sc}_{0.666-x}\text{Cl}_4$ series, a highly disordered Li^+ distribution was observed. It was then concluded that such disorder brought about a lattice with metastable intermediate Li^+ sites that enable a fast Li^+ diffusion and rate capability. The phase of $\text{Li}_2\text{In}_x\text{Sc}_{0.666-x}\text{Cl}_4$ series can be varied according to In^{3+} x contents. When x is between 0~0.444, the obtained $\text{Li}_2\text{In}_x\text{Sc}_{0.666-x}\text{Cl}_4$ is a cubic spinel phase with little impurity, as illustrated in Figure 3e, exemplified with spinel $\text{Li}_2\text{In}_{1/3}\text{Sc}_{1/3}\text{Cl}_4$. However, when x content goes higher, typically ≥ 0.555 , the fractions of monoclinic Li_3MCl_6 -typed phase and LiCl impurities begin to increase, as illustrated in Figure 3i, exemplified with spinel $\text{Li}_2\text{In}_{0.444}\text{Sc}_{0.222}\text{Cl}_4$ and Li_3ScCl_6 -typed $\text{Li}_3\text{In}_{2/3}\text{Sc}_{1/3}\text{Cl}_6$. The structure of $\text{Li}_2\text{In}_{1/3}\text{Sc}_{1/3}\text{Cl}_4$ (Figure 3f) is similar to the halospinel $\text{Li}_2\text{Sc}_{2/3}\text{Cl}_4$ [29] mentioned before, and also contains four Li^+ sites (with two new sites) per unit cell, though with different occupancies. From Figure 3f,g, one can readily see the significant Li^+ disorder as metastable intermediate Li sites that are supposed to benefit Li-ion mobility and fast rate capability. The face-shared Li2 octahedra and Li1 or Li3 tetrahedra with relatively low occupancies (~0.2–0.3) construct a 3D Li^+ migration pathway (Figure 3g,h). Benefiting from a relatively low activation energy (0.33 eV simulated from EIS measurements) for Li^+ diffusion, and 3D migration pathways (from BVSE calculation based on NPD Rietveld refinements) with considerable amounts of site vacancies (i.e., disorder, based on NPD Rietveld refinements), a high ionic conductivity of 2.0 mS cm^{-1} was finally achieved. As for Li_3ScCl_6 -typed monoclinic phase $\text{Li}_3\text{In}_{2/3}\text{Sc}_{1/3}\text{Cl}_6$ (Figure 3i), its main diffraction peaks overlapped with that of spinel $\text{Li}_2\text{In}_{0.444}\text{Sc}_{0.222}\text{Cl}_4$. One difference between the spinel $\text{Li}_2\text{In}_{0.444}\text{Sc}_{0.222}\text{Cl}_4$ and monoclinic $\text{Li}_3\text{In}_{2/3}\text{Sc}_{1/3}\text{Cl}_6$ is that, in spinel $\text{Li}_2\text{In}_{0.444}\text{Sc}_{0.222}\text{Cl}_4$ its Li4/Sc1/In1 metal sites are all shared (Figure 3j), but in monoclinic $\text{Li}_3\text{In}_{2/3}\text{Sc}_{1/3}\text{Cl}_6$ its Li1 sites and Sc1/In1 metal sites are all crystallographically distinct, that is, ordered (Figure 3k). In one word, this work can be seen as an intuitive illustration of how metal contents switch the cation arrangements between order and disorder.

3.3. Dual-Halogen and Lattice Dynamics

Tuning halogen anions in halides (F^- , Cl^- , Br^- , I^-) or introducing dual-halogen mixing can be an effective way to lower the Li^+ migration barrier, and improve moisture tolerance and electrode compatibility. In fact, this strategy of anion modulation involves changes on the polarizability of anions and the lattice. The host lattice polarizability can

affect the lattice vibration strength (that is, lattice dynamics) and correspondingly the Li^+ mobility kinetics, which has been rationalized by the Arrhenius equation [51] in which the activation barrier and prefactor are modulated. According to Wakamura et al.'s [52] study, low activation energies of Li^+ migration correspond to “low-energy” phonon frequencies (that is, low lithium vibration frequency) and a high frequency dielectric constant. From this perspective, a softer and more polarizable anion sublattice much favors a facile ionic transport. The polarizability of different metal cations and anions is shown in Table 1. It can be found that F^- has the lowest polarizability, and fluorides often exhibit low ionic conductivity (less than $10^{-5} \text{ S cm}^{-1}$). Bromide and iodide generally show higher polarizability than chloride, and hence higher ionic conductivity has been observed [21,53,54]. In one word, halogens with higher polarizability are expected to facilitate Li migration.

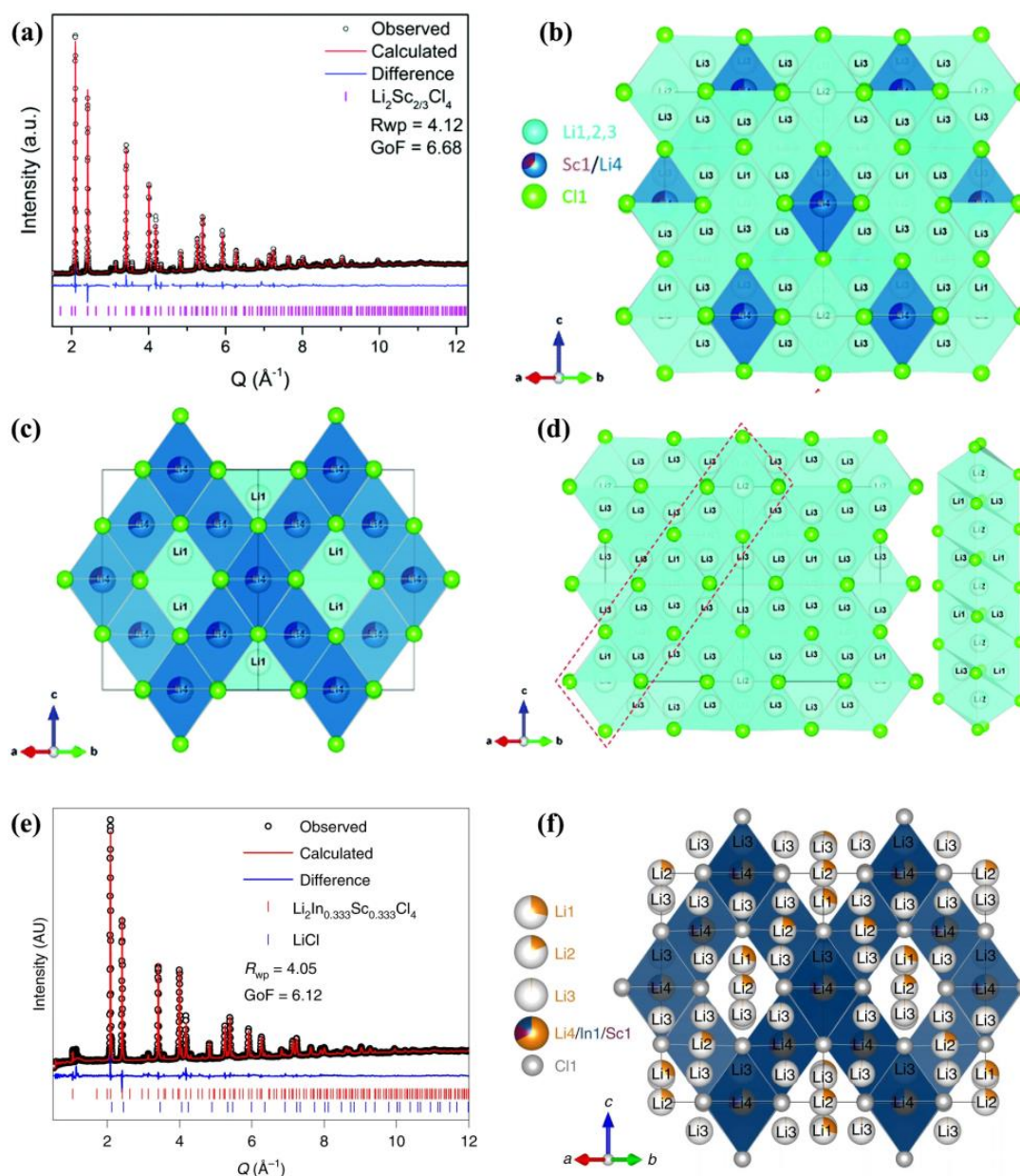


Figure 3. Cont.

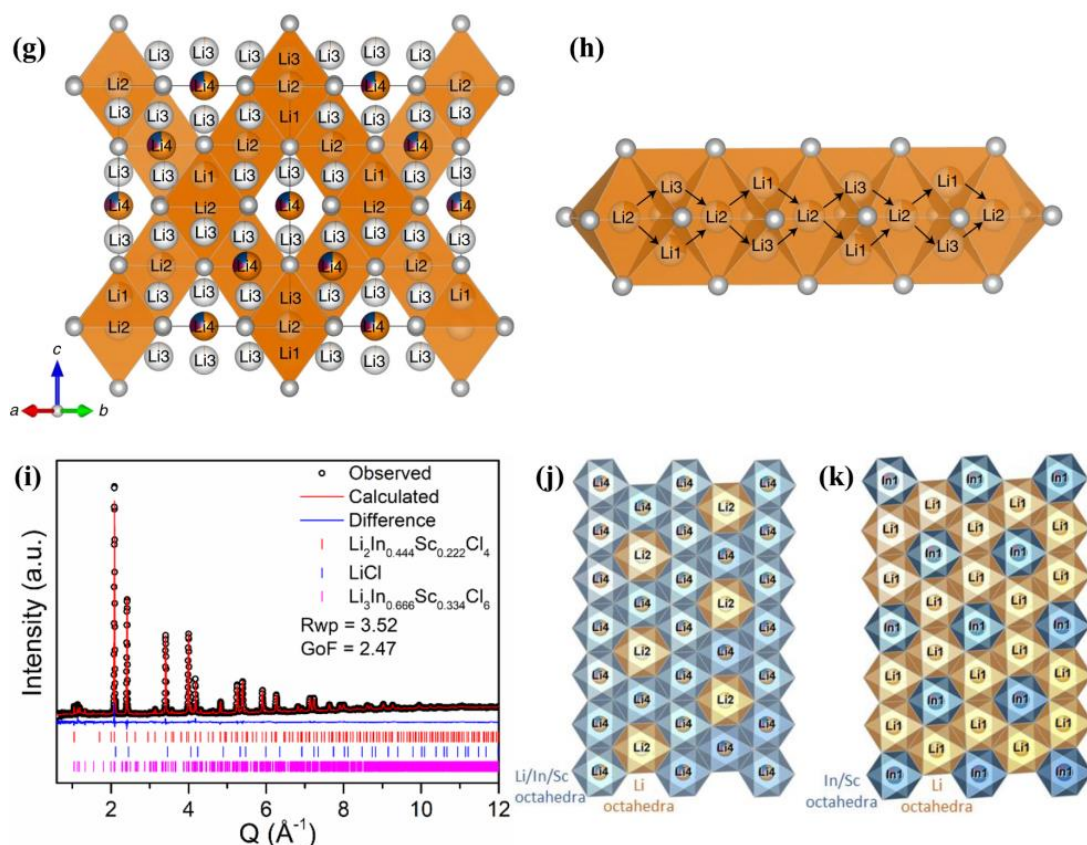


Figure 3. (a) Time-of-flight NPD Rietveld refinement on $\text{Li}_2\text{Sc}_{2/3}\text{Cl}_4$. (b) Structure of disordered spinel $\text{Li}_2\text{Sc}_{2/3}\text{Cl}_4$. (c) Structure without showing Li_2 octahedra and Li_3 tetrahedra. One can see that it basically has a Li_2MgCl_4 -typed structure framework but with different site occupancies. (d) Li^+ diffusion pathway of $\text{Li}_2\text{Sc}_{2/3}\text{Cl}_4$ along the face-shared Li_1 , Li_3 tetrahedra and Li_2 octahedra; right inset is the expansion of the red dot area illustrating a potential diffusion pathway through Li_2 octahedra and Li_1 , Li_3 tetrahedra. Reproduced with permission: Copyright 2020, Royal Society of Chemistry [29]. (e) TOF NPD Rietveld refinement of $\text{Li}_2\text{In}_{1/3}\text{Sc}_{1/3}\text{Cl}_4$. (f) Structure of $\text{Li}_2\text{In}_{1/3}\text{Sc}_{1/3}\text{Cl}_4$ viewed as only $\text{Li}_4/\text{In}_1/\text{Sc}_1$ octahedral framework. (g) Li^+ diffusion pathway via face-shared Li_1 tetrahedra and Li_2 octahedra. (h) Enlarged Li^+ diffusion pathway through Li_2 octahedra and adjacent Li_1 or Li_3 tetrahedra. (i) NPD Rietveld refinements with spinel $\text{Li}_2\text{In}_{0.444}\text{Sc}_{0.222}\text{Cl}_4$ and monoclinic $\text{Li}_3\text{In}_{0.666}\text{Sc}_{0.334}\text{Cl}_6$. (j) Illustration of spinel structure in which $\text{Sc}/\text{In}/\text{Li}$ sites are all shared. (k) Illustration of monoclinic structure in which In/Sc and Li sites are distinct. Reproduced with permission: Copyright 2022, Springer Nature [50].

Bearing this in mind, Liu et al. [55] utilized bromide with higher polarizability to make an anion-mixed halide $\text{Li}_3\text{Y}(\text{Br}_3\text{Cl}_3)$ via the hot-pressing method to promote conductivity, along with optimization on the grain boundary. Conventionally, Li_3Cl_6 yields the trigonal phase while Li_3YBr_6 yields the monoclinic phase. The ball-milled $\text{Li}_3\text{Y}(\text{Br}_3\text{Cl}_3)$ was initially a mixture of Li_3YCl_6 and Li_3YBr_6 . However, after hot-pressing, the $\text{Li}_3\text{Y}(\text{Br}_3\text{Cl}_3)$ mixture transformed into a single Li_3YBr_6 -type monoclinic phase and then reached a strikingly high conductivity of 7.2 mS cm^{-1} (room-temperature). The author then ascribes this to the high occupancy of tetrahedral Li sites and the optimized contact between grain boundaries that resulted from the hot-pressing method.

NPD refinement (Figure 4a) clearly confirmed the whole structure and the significant amounts of additional tetrahedral Li sites (cyan sphere in Figure 4b) in the lattice. The refinement was completed on the basis of the Li_3YBr_6 structure model with half of the Br replaced by Cl . The whole structure consists of a transition metal chloride layer and lithium chloride layer (Figure 4c). In the metal chloride layer, Li^+ ions partially occupy the Y^{3+}

ions' position to form a honeycomb-type local ordering of YX_6 and LiX_6 ($X = Br$ and Cl) octahedra (Figure 4d), along with some vacancies on both sites. This honeycomb ordering has been mentioned above [40,41], and is also similar to Li-Mn rich cathode materials [56]. Moreover, a stacking faults along the c -axis could be confirmed by NPD refinements on 5.5~6 Å data, representing a long-range disorder of the honeycomb's location along the c -axis, which is also observed in layered oxide $Na(Ni_{2/3}Sb_{1/3})O_2$ [57].

The above-mentioned tetrahedral Li sites are actually located by an NPD Difference Fourier map (cyan sphere in Figure 4b). We have mentioned this Difference Fourier procedure in Section 2.3; it is very effective in locating residue density which probably represents missing Li^+ ions. Four different tetrahedral sites (pink sphere in Figure 4c,e,f), with two sites in the lithium layer and the other two in the transition metal layer, were successfully located using this procedure. They were found to coexist with Li^+ octahedral sites in their lithium chloride layer. However, the author mentioned that the residual densities on these sites probably result from the presence of stacking faults along the c -axis, and some of them are very likely to be empty tetrahedral sites due to repulsion from Y^{3+} ions [16,21] (Figure 4e,f). Through BVSE calculation [36,37], the author proposed that the presence of these tetrahedral Li^+ sites (marked as "T-Li at 8j site") depopulates the octahedral Li^+ occupancies (that is, creates more vacancies); in which case, it brings about a more flat energy landscape for a concerted Li^+ diffusion. Such Li^+ distribution enables an octahedra–tetrahedra–octahedra (O-T-O) Li^+ hopping chain along the a -direction, which is then connected by octahedral sites ($2d$) to form a 2D diffusion network in the ab -plane (Figure 4e). Along the c -direction, hopping along an "O-T-O-T" zigzag route nearby Y^{3+} sites is allowed, which fulfills a 3D diffusion pathway (Figure 4f). In a word, tetrahedral Li^+ lowers the diffusion activation energy in the ab -plane and promotes O-T-O-T zigzag diffusion along the c -direction.

In addition, the low resistance grain boundaries as formed during hot-pressing are also beneficial to conductivity enhancements. Such boundaries are proposed to originate from partial melting during the hot-pressing process, and the formation of fused grain boundaries might be relevant to the eutectic melting of multiple halide components. This study indicates that these anion-mixed halides have higher than expected potential as promising SSEs. Their easy-forming fused grain boundaries are quite advantageous in large scale fabrication.

However, the incorporations Br and I would lower the oxidation stability according to thermodynamic calculation. Therefore, one needs to carefully consider the trade-off between high ionic conductivity and good stability, and try to balance these two by delicately controlling the ratio of halogens. Bearing this in mind, Maas et al. [58] delicately designed the Cl/Br ratio in a $Li_3YBr_xCl_{6-x}$ system and successfully realized the above. They found that Br^- -rich halides are more conductive (5.36×10^{-3} S/cm at 30 °C for $Li_3YBr_{4.5}Cl_{1.5}$) but less oxidative stable (~ 3 V) compared to Li_3YCl_6 (~ 3.5 V). Thus, they introduced only a small quantity of Br^- in the halide, that is $Li_3YBr_{1.5}Cl_{4.5}$, to keep its oxidative stability unaffected but make its ionic conductivity substantially improved (2.1×10^{-3} S/cm at 30 °C), compared to pristine Li_3YCl_6 (0.049×10^{-3} S/cm at 30 °C). Neutron diffraction refinement (Figure 4g,h) revealed that as Br contents increase, a phase transition happens, from the $P-3m1$ trigonal phase of $Li_3YBr_xCl_{6-x}$ at $x = 0, 1.5$ with hexagonal close-packing (hcp) lattice, to monoclinic $C2/m$ phase of $Li_3YBr_xCl_{6-x}$ at $x = 3, 4.5, 6$ with a cubic close-packing (ccp) lattice. In all series, Br and Cl were randomly distributed on halogen sites. This study highlights that appropriate modulation of halogen substituents in the anion framework to optimize the balance between conductivity and stability is reasonable and feasible.

Regardless of oxidative stability, using iodine to yield the possibly largest polarizability in a halide lattice would provide a good chance for studying lattice polarizability effects. Schlem et al. [54] report the first experimentally obtained iodine-based halide superconductor Li_3ErI_6 , of which the Li^+ ionic conductivity is close to 1 mS cm^{-1} . In their work, Iodine (I) was adopted as a more-polarization anion to make a softer lattice of Li_3ErI_6 compared to Li_3ErCl_6 . Using NPD, they performed a thorough investigation of the highly polarized

lattice and the transport mechanism. Through their investigation of the Debye frequency of the lattice and impedance spectroscopy, they corroborated that improved ionic transport results from the iodide anion induced softer and more polarizable framework. Their results demonstrate that the idea of softer lattices also holds up in this class of materials.

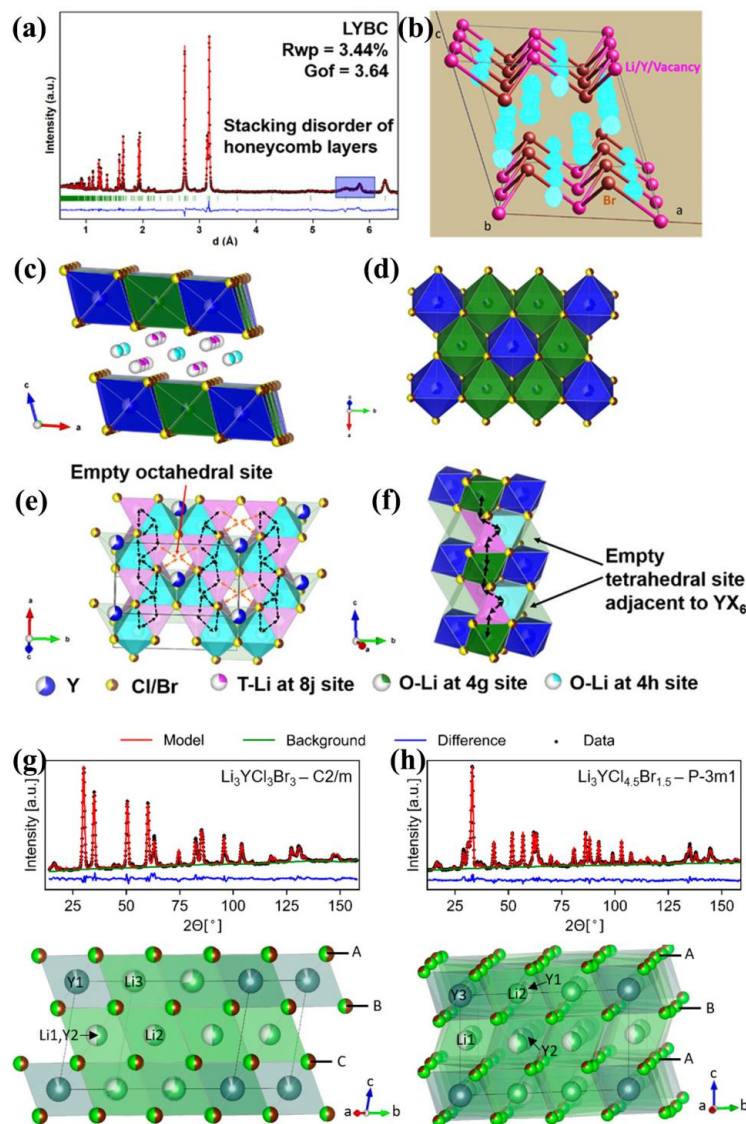


Figure 4. (a) NPD Rietveld refinement of hot-pressed $\text{Li}_3\text{Y}(\text{Br}_3\text{Cl}_3)$. Black dots are observed data, red lines are simulated data. (b) Fourier difference map based on NPD Rietveld refinements of hot-pressed $\text{Li}_3\text{Y}(\text{Br}_3\text{Cl}_3)$. The light-blue spheres represent the tetrahedral Li sites. (c,d) Monoclinic structure of hot-pressed $\text{Li}_3\text{Y}(\text{Br}_3\text{Cl}_3)$ shown in different directions. (e,f) Li^+ diffusion pathways depicted by black and red arrows in ab -plane and along c -direction. Reproduced with permission: Copyright 2020, American Chemical Society [55]. (g,h) Neutron powder diffraction of monoclinic and trigonal phase. Their corresponding structure are shown below. Reproduced with permission: Copyright 2022, Royal Society of Chemistry [58].

Refinements on NPD and Synchrotron diffraction data are shown in Figure 5a,b. Li_3ErI_6 resembles a new monoclinic structure (space group $C2/c$). Synchrotron diffraction data was firstly refined to identify the lattice parameters, space group, Er^{3+} , I^- ion positions and their thermal displacements. Later, NPD was refined to determine the coordinates and thermal displacements of Li^+ . The final structure (Figure 5c,d) consists of isolated layers of edge-shared ErI_6^{3-} octahedra, with LiI_6^{5-} octahedra interlayers between them. Er^{3+} partially occupies two different Wyckoff positions ($8f$, $4d$) with remarkably different

occupancies, which can be seen as a rare-earth cation disorder. Interestingly, the Li^+ ions also occupy these partially vacant Er^{3+} sites, resulting in a Li^+ - Er^{3+} disorder within these layers. Essentially, the structure can be seen as alternating layers of Er/Li co-occupied edge-shared $[\text{Er}_x\text{Li}_{(1-x)}\text{I}_6^{(5-2x)^-}]$ octahedra (on Wyckoff 8f, 4d sites) and edge-sharing $[\text{LiI}_6^{5-}]$ octahedra (on Wyckoff 4e sites). In addition, through BVSE calculation [36,37] a two-dimensional Li^+ diffusion pathway in the *ab* plane has been revealed (Figure 5e,f). The beige isosurface corresponds to the possible Li^+ residence representing diffusion pathway. The blue section of this isosurface in the *ab*-plane is to show the interconnectivity of Li^+ residence. Note that the interstitial tetrahedral voids and vacant octahedral sites (Figure 5f) could both serve as transition-sites for Li^+ diffusion.

Incorporating I^- anion could soften the lattice and decrease the entropy of migration, which is correlated with the activation barrier as rationalized by the Arrhenius prefactor of the ionic conductivity [59]. The author conducted speed of sound measurements and found that from Li_3ErCl_6 (for comparison) to Li_3ErI_6 , the longitudinal, transverse, mean speed, and calculated Debye frequencies, all decrease. Such a decline reflects the weakening in average bond strength and increase in bond length. Hence, the iodide anions indeed bring a softer anionic framework in Li_3ErI_6 . Li_3ErI_6 shows a lower prefactor σ_0 , lower activation barriers E_a and higher room-temperature conductivity σ_{RT} as a function of Debye frequency.

Finally, fluorine substitution was also reported by Tang et al. [60]. They successfully fabricated a dual-halogen trigonal $\text{Li}_2\text{ZrCl}_{6-x}\text{F}_x$. Admittedly, among all halogens, fluorine has the least polarizability and strongest electronegativity, leading to inferior conductivity. However, a fluorine substitution strategy has been proposed to inhibit interfacial reaction against electrodes and moisture corrosion owing to its strong electronegativity [61,62]. Therefore, similar to the above-mentioned Cl-Br mixing [58], a trade-off between conductivity and stability has been investigated by Tang et al. [60] in their $\text{Li}_2\text{ZrCl}_{6-x}\text{F}_x$ system.

Dual-halogen trigonal $\text{Li}_2\text{ZrCl}_{6-x}\text{F}_x$ systems have considerable moisture stability and excellent electrode compatibility. In their optimal $\text{Li}_2\text{ZrCl}_{6-x}\text{F}_x$ ($x = 0.4$), there are three crystallographic Cl^- sites, and the F^- occupancies on these three sites are a little different: that is 7.9%, 8.5% and 4.8% on the Cl1 (6i), Cl2 (6i) and Cl3 (6i) sites, respectively, as confirmed by NPD refinements shown in Figure 5g. The refined structure is shown in Figure 5h,i, in which $\text{Li}_2\text{ZrCl}_{6-x}\text{F}_x$ ($x = 0.4$) adopts a trigonal hcp anion stacking, forming $[\text{LiX}_6]$ and $[\text{ZrX}_6]$ ($X = \text{Cl}, \text{F}$) octahedral with vacancies. There are two Li sites along the *c*-direction, one occupies about 3/4 of the Li1 layer on (001) planes, and the other one almost fully occupies the Li2 layer on (002) planes. Each ZrX_6^{3-} octahedron is surrounded and connected by six LiX_6^{5-} octahedra in an edge-shared manner that forms a honeycomb arrangement in the *ab*-plane.

However, since the F-Li bond is stronger and its bond length is shorter than Cl-Li, F substitution will cause Li^+ octahedra distortion along with lattice contraction, which would reversibly increase the Li^+ migration energy barrier and decrease ionic conductivity. Therefore, the fluorine contents have to be carefully controlled and the best one is $\text{Li}_2\text{ZrCl}_{6-x}\text{F}_x$ ($x = 0.4$), which retains an ionic conductivity of $3.21 \times 10^{-4} \text{ S cm}^{-1}$ that is very close to non-fluorine Li_2ZrCl_6 (Figure 5j). Moreover, $\text{Li}_2\text{ZrCl}_{6-x}\text{F}_x$ can be applied to protective-layer-free ASSLBs with a lithium alloy anode and high-voltage cathode LiCoO_2 . These cells were reported to have an initial coulombic efficiency as high as 95.57%, and to be able to reversibly cycle in a wide potential window from 2.52 to 4.32 V (versus Li^+/Li). The author concluded that a self-passivating behavior of $\text{Li}_2\text{ZrCl}_{6-x}\text{F}_x$ SSE occurring on its contacting surface against the Li alloy anode was found to be responsible for its interfacial stabilization. The thin solid-electrolyte interphase (SEI) layers containing LiCl and LiF as a passivating layer would prevent $\text{Li}_2\text{ZrCl}_{6-x}\text{F}_x$ from decomposition by limiting its electron transfer, but it still allows facile Li^+ transport. In addition, the stronger stability against moisture in LZCF could originate from robust Li-F and Zr-F bonds due to more electronegativity of F^- .

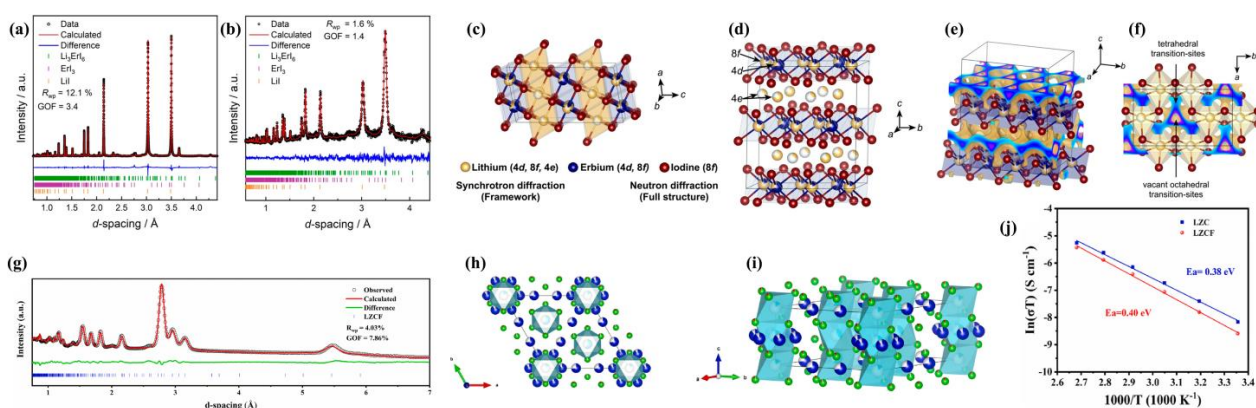


Figure 5. Rietveld refinements on (a) synchrotron diffraction data and (b) NPD data with the monoclinic $C2/c$ structure of Li_3ErI_6 . (c,d) Refined crystal structure of Li_3ErI_6 , showing alternating layers of $[\text{Er}_x\text{Li}_{(1-x)}\text{I}_6^{(5-2x)-}]$ and $[\text{Li}_6^{5-}]$ octahedra. (e) BVSE [36,37] calculation for possible Li^+ migration pathway. The beige isosurface is actually an electrostatic estimation. It means the probable lithium residence and lithium diffusion pathway. The blue section in the ab -plane is to show the strongly interconnected nature of Li sites, possibly related to a fast in-plane diffusion. (f) Tetrahedral voids are adjacent to edge-shared LiI_6^{5-} octahedral. Both the voids and octahedral vacancies may act as transitional states for Li^+ diffusion. Reproduced with permission: Copyright 2022, American Chemical Society [54]. (g) Rietveld refinement of the NPD data for the $\text{Li}_2\text{ZrCl}_{6-x}\text{F}_x$ ($x = 0.4$). (h,i) The crystal structure obtained from above refinement. The blue, cyan, green and red balls represent Li, Zr, Cl and F, respectively. (j) Arrhenius plots of $\text{Li}_2\text{ZrCl}_{6-x}\text{F}_x$ ($x = 0.4$) (LZCF) and Li_2ZrCl_6 (LZC). Reproduced with permission: Copyright 2023, Elsevier [60].

3.4. Structure Determination in New Halide System

In search of SSEs, it would be very exhilarating to discover a novel halide system as a promising SSE to support the ASSB battery. In fact, this crystalline novel halide system strongly needs NPD to reveal its inner mechanism. Utilizing NPD data to solve its unprecedented structure with an unconventional Li sublattice is also a good reflection of NPD's superiority. Here we take a recently reported new LaCl_3 -based halide system [63] as an example to discuss NPD's role in this study.

Yin et al. [63] have made shocking progress on a new LaCl_3 -based halide system as a lithium superionic conductor, which possesses promising interfacial electrochemical compatibility with lithium metal anodes. According to their report, unlike conventional Li_3MCl_6 ($M = \text{Sc}, \text{Y}, \text{In}, \text{and Ho}$) [21,22,26,42], this halide system possesses a UCl_3 -type LaCl_3 structure with large 1D channels that enable fast Li^+ conduction. These 1D channels are interconnected via La vacancies induced by Ta doping, in which case a 3D Li^+ migration network is established. In their optimized $\text{Li}_{0.388}\text{Ta}_{0.238}\text{La}_{0.475}\text{Cl}_3$, the Li^+ ionic conductivity (at 30°C) is as high as 3.02 mS cm^{-1} and the activation energy is as low as 0.197 eV . It also fulfills a long-term cycling in Li symmetric cell with 1 mAh cm^{-2} for more than 5000 h. The author ascribed such stability to the gradient interfacial passivation layer that helps stabilize the Li metal electrode. It is also reported that, under a cutoff voltage of 4.35 V and with the areal capacity of more than 1 mAh cm^{-2} , the battery with $\text{Li}_{0.388}\text{Ta}_{0.238}\text{La}_{0.475}\text{Cl}_3$ SSE assembled with a Li metal anode and uncoated $\text{LiNi}_{0.5}\text{Co}_{0.2}\text{Mn}_{0.3}\text{O}_2$ cathode can run for more than 100 cycles. Rapid Li^+ conduction was also demonstrated in this lanthanide-based system (LnCl_3 ; $\text{Ln} = \text{La}, \text{Ce}, \text{Nd}, \text{Sm}$ and Gd).

Neutron powder diffraction has played an indispensable role in this inspiring work, especially in determining the new crystal structure with explicit Li distribution/occupation, and elucidating the Li migration pathway, which provides a fundamental understanding of structural design for property enhancements. Figure 6a,b provide a joint refinement of synchrotron X-ray and Neutron diffraction. The synchrotron X-ray identifies Ta, La, Cl, especially La/Ta vacancies to confirm the whole lattice framework, while the neutron data

confirm lithium distribution. We can see that neutron data ranges from approximately 0.28 \AA ($Q \sim 3.6 \text{ \AA}^{-1}$) to 0.1 \AA ($Q \sim 9.6 \text{ \AA}^{-1}$). Such low d -spacing data is especially beneficial in determining the local coordination environment and Li^+ disorder.

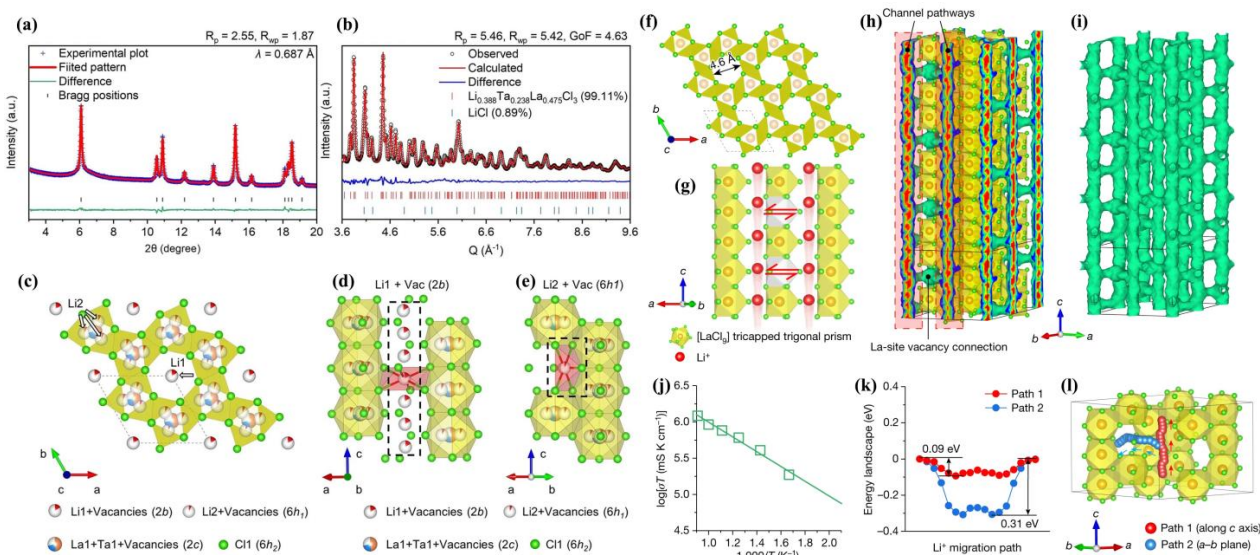


Figure 6. Joint refinements on (a) synchrotron diffraction data (wavelength 0.687 \AA) and (b) TOF NPD data. (c) Refined structure of $\text{Li}_{0.388}\text{Ta}_{0.238}\text{La}_{0.475}\text{Cl}_3$ viewed along c -axis. (d) Coordination conditions of Li1. The red polyhedrons stand for $[\text{LiCl}_6]$ polyhedron. (e) Coordination environment of Li2 site. The $[\text{LiCl}_5]$ polyhedron is marked in red. It should be emphasized that the ions' positions only reflect the averaged probability of residence, not real existence of ions. (f) View along c -direction of the LaCl_3 lattice. The inner diameter of the channel is around 4.6 \AA . (g) Side view of the vacancy-contained LaCl_3 lattice. The Li^+ ions could migrate along the 1D channel (red spheres) and cross the channel (bidirectional red arrows) via vacant octahedra (grey). (h) AIMD-simulated green isosurfaces representing Li^+ probability density (at 900 K) (i) Isolated Li^+ probability density isosurfaces in which all $[\text{LaCl}_9]$ polyhedrons are omitted to give a clear view of the interconnectivity of the diffusion pathways. (j) AIMD-simulated Arrhenius plot of Li^+ diffusion at selected temperature points. (k,l) Li^+ migration pathways and energy barriers. The migration along the 1D channel in the c -direction is shown in red as path 1, and the migration across the adjacent channels are shown in blue as path 2. Reproduced with permission: Copyright 2023, Springer Nature [63].

The lattice presents a UCl_3 -type structure with $P6_3/m$ space group (Figure 6c–e), possessing a channel-typed non-close-packed anion lattice different from hcp Li_3YCl_6 and ccp Li_3InCl_6 types [21,22,26,42]. La^{3+} vacancies were clearly found after introducing Ta^{5+} . Two Li^+ positions were found, namely Li1 and Li2, along with their surrounding Cl^- constituting the compressed $[\text{Li}_1\text{Cl}_6]$ octahedra in the channels and $[\text{Li}_2\text{Cl}_5]$ rectangular pyramids near La sites. The author mentioned that 6h1 is an intermediate Li site in a metastable state that is critical in supporting the Li^+ fast motion across adjacent channels. Figure 6f clearly shows 1D channels constructed by six columns of edge-shared $[\text{LaCl}_9]$ tricapped trigonal prisms in the LaCl_3 lattice. Its large inner diameter around 4.6 \AA offers a wide space that accommodates abundant octahedral sites for Li^+ ionic motion. The author further proposed that 1D channels are interconnected by La vacancies to form a 3D Li-diffusion lattice, as shown in Figure 6g. The lithium not only migrates along the 1D channel but also migrates to the neighboring one via La vacancies sites. This could be supported by bond valence site energy (BVSE) analysis [36,37] on the basis of an NPD-determined structure. Finally, BVSE calculation illustrates an energetically favored 1D diffusion chain $[\text{Li}_1\text{–Li}_2\text{–Li}_1]$ along the c -direction, with an energy barrier of merely 0.18 eV that is much lower than that of 0.5 eV for diffusion across adjacent channels via La vacancies.

Ab initio molecular dynamics (AIMD) simulations also confirm a fast Li^+ transport along a spread of closely spaced sites in the 1D channels (Figure 6h). The irregularly elongated Li^+ probability density was suggested to be related to Li^+ site disordering, which was considered to be a crucial factor to fulfill rapid Li^+ conduction [64]. The Li^+ could migrate between adjacent channels via La vacancies (Figure 6h). The interconnected 3D Li^+ diffusion pathway is depicted in Figure 6i (all polyhedrons are omitted). The AIMD simulation yields a calculated ionic conductivity as high as 13.8 mS cm^{-1} at 300 K (Figure 6j). The energy landscape in Figure 6k clearly illustrates two different Li^+ diffusion pathways, with an energy barrier of 0.09 eV along the c -direction channels (red path in Figure 6k,l), and an energy barrier of 0.31 eV across channels in the a - b plane (blue path in Figure 6k,l). Both values are lower than the above BVSE results. These results imply that La^{3+} vacancies, which mainly originate from Ta^{5+} doping, are of vital importance to endow the LaCl_3 lattice with a rapid Li^+ conduction.

These unique structure features and interconnected migration pathways allow the halide system to reach its best ionic conductivity σ of 3.02 mS cm^{-1} (at 30°C) in $\text{Li}_{0.388}\text{Ta}_{0.238}\text{La}_{0.475}\text{Cl}_3$. It also exhibits an excellent electrode compatibility that allows stable cycling with an areal capacity of 1.16 mAh cm^{-2} in $\text{Li}/\text{Li}_{0.388}\text{Ta}_{0.238}\text{La}_{0.475}\text{Cl}_3/\text{NCM523}$ full cell. This research also manifests the superiority of the electrode compatibility of LaCl_3 -based SEs. It can be expected that this work in future will inspire far more investigation of this brand new UCl_3 -type SSE system of LnCl_3 lattice with multiple element-doping choices.

3.5. In Situ NPD Study on Phase Evolution (Transition)

In situ NPD can directly monitor the dynamics process of phase evolution (or transition). The in situ NPD utilization discussed here mainly involves phase analysis during the dehydration process and heating process. The first work on dehydration analysis comes from an investigation on Li_3InCl_6 humidity tolerance and degradation. The second work on heating analysis come from an investigation of Li_2ZrCl_6 thermal stability.

In terms of humidity tolerance, it has been acknowledged that most SSEs will degrade when exposed to ambient air [65–67]; however, Li_3InCl_6 appears to possess much stronger humidity tolerance than others [30], along with high ionic conductivity and high voltage compatibility [22,23]. According to Li et al.'s study [30], Li_3YCl_6 is unstable even in low humidity, and will decompose to simple chloride hydrates $\text{LiCl}\cdot\text{H}_2\text{O}$ and $\text{YCl}_3\cdot 6\text{H}_2\text{O}$ after exposure in air for 12 h with 3–5% humidity. This decomposition cannot be recovered by reheating in an inert atmosphere. However, when introducing certain amounts of In^{3+} into Li_3YCl_6 , the humidity tolerance was significantly improved. This is because $\text{Li}_3\text{Y}_{1-x}\text{In}_x\text{Cl}_6$ (with $x > 0.5$) [30] and also Li_3InCl_6 after humidity exposure can form $\text{Li}_3\text{Y}_{1-x}\text{In}_x\text{Cl}_6\cdot\text{H}_2\text{O}$ and $\text{Li}_3\text{InCl}_6\cdot\text{H}_2\text{O}$ intermediates rather than decompose to simple chloride hydrates. More importantly, the $\text{Li}_3\text{Y}_{1-x}\text{In}_x\text{Cl}_6$ SSEs could be regained after reheating at 260°C . The above results demonstrate that high In^{3+} contents could help to retain the $(\text{Y}/\text{In})\text{Cl}_6^{3-}$ octahedral frameworks after humidity exposure by forming hydrated intermediates, which could then be regenerated after a careful dehydration process.

Since $\text{Li}_3\text{Y}_{1-x}\text{In}_x\text{Cl}_6$ (with $x > 0.5$) and Li_3InCl_6 all adopt a ccp monoclinic structure rather than hcp orthorhombic structure as in Li_3YCl_6 , we deduce that the stronger humidity tolerance is possibly related to this ccp monoclinic structure that is able to accommodate water molecules in the lattice without being broken. This is also a possible explanation why Li_3InCl_6 can be synthesized via a water-mediated route followed by controlled dehydration [23].

Nevertheless, there is still some remaining further debate. For instance, how does the phase change during dehydration? Why does the conductivity of reheated $\text{Li}_3\text{Y}_{1-x}\text{In}_x\text{Cl}_6$ not fully recover after dehydration (retention: 85.37% for $\text{Li}_3\text{Y}_{0.2}\text{In}_{0.8}\text{Cl}_6$, 87.22% for $\text{Li}_3\text{Y}_{0.1}\text{In}_{0.9}\text{Cl}_6$)? Apparently, deciphering the dehydration/tolerance process in this halide system could be of much significance.

Bearing this in mind, the first work discussed here is about the in situ NPD/XRD study of the dehydration process of Li_3InCl_6 (that is from $\text{Li}_3\text{InCl}_6 \cdot 1.5\text{H}_2\text{O}$ to pure Li_3InCl_6) conducted by Sacci et al. [44]. They emphasize that careful consideration should be taken during the dehydration process and a strong vacuum is indispensable. In situ NPD revealed that the dehydration process actually involves multiple phase transitions that could significantly vary the conductivity. The lithium conductivity can be related to the amount of residual H_2O , the structural stability and ordering of the lithium sublattice.

As shown in Figure 7a,c, in situ XRD measurements detected two sets of diffraction peaks upon heating, which represents a single transition of the host framework from the fully hydrated to the anhydrous phase. The hydrate $\text{Li}_3\text{InCl}_6 \cdot 1.5\text{H}_2\text{O}$ can maintain from 30 to 80 °C, which bears a $P2_1/c$ space group. Above 80 °C, the anhydrous phase appears with a $C2/m$ space group, and the remaining hydrate transforms to anhydrate rapidly between 110 and 150 °C. However, under in situ neutron diffraction (Figure 7b) (deuterated water is used in sample synthesis), at least four distinct phases could be identified with overlapping on their temperature ranges. The reason for this is that XRD lacks sensitivity with light elements like Li or H, so that structural changes in the Li sublattice would not be observed. The variation of neutron data demonstrates that, as they dehydrate, the sublattices of Li^+ and H^+ are drastically modulated. Note that in neutron data the transition from phase 2 ($\text{Li}_3\text{InCl}_6 \cdot x\text{H}_2\text{O}$) to 3 ($\text{Li}_3\text{InCl}_6 \cdot 0.5\text{H}_2\text{O}$) also occurs above 80 °C. This coincides well with the XRD transition temperature and the conductivity boost. Since not much change is observed in XRD above 90 °C, this means that the In and Cl host frameworks basically lock in above 90 °C. In other words, the In–Cl octahedra support the layered structure frameworks for H_2O and Li ions to reside within.

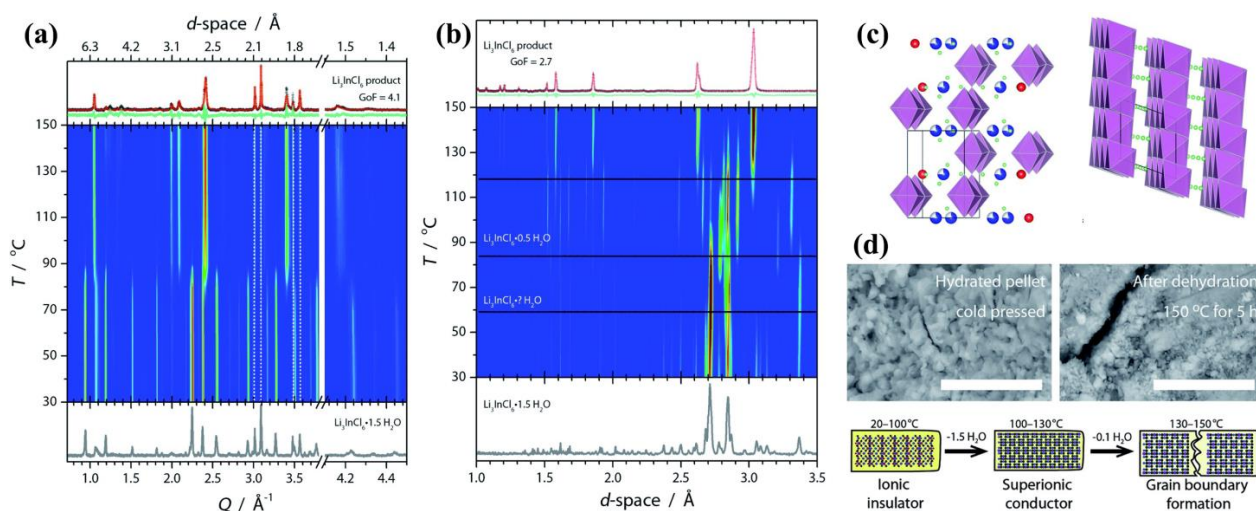


Figure 7. (a) In situ XRD data and (b) In situ NPD data of Li_3InCl_6 collected during vacuumed dehydration process. Each temperature step is held for 45 min for data collection, with a temperature scanning rate of $1\text{ }^\circ\text{C min}^{-1}$. Top patterns are the refinements for the dehydrated Li_3InCl_6 , in which black dots are observed data, red lines are simulated data, green lines are difference. (c) Crystal structures viewed along different directions for the hydrated (left) and anhydrous (right) Li_3InCl_6 phases. InCl_6^{3-} octahedra are shown in purple; Li ions are in green; chloride ions are in blue, with partial occupancies; oxygen ions are in red sphere. (d) SEM of a pellet cross section. Scale bar is $10\text{ }\mu\text{m}$. The inset below is the proposed evolution of particle, grain boundary and structure of Li_3InCl_6 hydrate during heating in vacuum. Reproduced with permission: Copyright 2021, Royal Society of Chemistry [44].

As the remaining H_2O is further removed, Li transport becomes more facile, and reaches its maximum when water molecules are totally removed. Subsequent cooling in the absence of water makes no observable change on the ionic conductivity, demonstrating that water molecules in the hydrate lattice are the main cause for its inferior conductivity. Dehy-

dration is accompanied by pellet contraction, with the observation of clear grain boundary formation shown in Figure 7d. The dehydrate Li_3InCl_6 exhibits orders of magnitude higher conductivity ($1.1 \times 10^{-3} \text{ S cm}^{-1}$) than hydrate $\text{Li}_3\text{InCl}_6 \cdot 1.5\text{H}_2\text{O}$ ($3.5 \times 10^{-7} \text{ S cm}^{-1}$). The author concludes that the presence of H_2O molecules would probably extend the required Li^+ or block the original facile Li^+ transport pathway, and eventually lead to the decrease in Li mobility.

The grain boundary as formed during dehydration (Figure 7d) may be one reason that the above-mentioned reheated $\text{Li}_3\text{Y}_{1-x}\text{In}_x\text{Cl}_6$ [30] fails to fully recover its ionic conductivity. Although dehydration of the hydrate is a feasible and facile synthesis route toward Li_3InCl_6 , the final removal of trace H_2O would inevitably lead to stress fractures and therefore the formation of the grain boundary. It may be possible to alleviate grain boundaries' formation by careful control of the dehydration rate or exertion of mechanical pressure. The author finally emphasized that the control of the as-formed grain boundary implies high-throughput processing during roll-to-roll fabrication of solid electrolytes.

The second work is about the in situ NPD analysis of the phase transition of Li_2ZrCl_6 [68] while heating. The Li_2ZrCl_6 (LZC) system generally preserves high humidity tolerance, good deformability, excellent compatibility with 4V-class cathodes, and significantly low cost in terms of the raw materials. Unlike Li_3InCl_6 , Li_2ZrCl_6 undergoes neither moisture uptake nor conductivity deterioration after being exposed to the atmosphere with 5% relative humidity. However, it undergoes phase transition during heating. As reported by Wang et al. [68], two type of Li_2ZrCl_6 (LZC) phases exist, i.e., trigonal α -LZC from ball-milling (without calcined) and monoclinic β -LZC from annealing at 350°C . Trigonal α -LZC has higher room-temperature ionic conductivity ($8.08 \times 10^{-4} \text{ S cm}^{-1}$).

Phase transition from trigonal α - to monoclinic β -LZC occurs above 277°C , accompanied by a decrease in conductivity. After annealing at 350°C , the ionic conductivity of LZC at 25°C will decrease by two orders of magnitude, that is, from $8.08 \times 10^{-4} \text{ S cm}^{-1}$ of α -LZC, to $5.81 \times 10^{-6} \text{ S cm}^{-1}$ of β -LZC. The XRD and in situ NPD analysis (Figure 8a,b) reveal a α -LZC phase below 277°C , and the coexistence of α - and β -LZC phases from 277°C to 350°C . Above 350°C , only β -LZC could be observed, and above 450°C the LZC would melt. The α -LZC is isostructural to Li_3YCl_6 (space group $P-3m1$, trigonal), while β -LZC is isostructural to Li_3InCl_6 , (space group $C2/m$, monoclinic). Considering that the material annealed at 350°C , then followed by furnace cooling, still maintains a pure β -LZC structure (Figure 8a) rather than turning into α -LZC structure, it could be deduced that α -LZC is likely a metastable phase originating from the high energy planetary mill. This is the quite distinctive to other chlorides in which planetary mill can only change the crystallinity rather than the crystal structure [21,22,30].

Through NPD refinements (Figure 8c), they found that Li^+ ions in as-milled α -LZC prefer to occupy 6h sites (Figure 8d), but in contrast, in Li_3YCl_6 two Li sites (6g and 6h) are both well-occupied (occupancy > 0.50) [21]. The BVSE method [36,37] calculates the migration pathway and energy barrier (Figure 8e–l). For α -LZC, the most energetically favorable diffusion pathway is the [Li1–Li2–Li1] chain along the c -direction, as marked in red in Figure 8f–h. Beside this diffusion chain, Li^+ is also likely to diffuse along the [Li1–i1–Li1–i2–Li1] pathway (i represents the interstitial site), or [Li2–i3–Li2] pathway, as marked in blue and green, respectively, in Figure 8f–h. These two alternative pathways could link the above [Li1–Li2–Li1] chains to establish a 3D diffusion network, of which the migration barrier is 0.803 eV (Figure 8g,h). For the β -LZC structure (Figure 8i), the relatively favorable Li^+ pathways reside within the layers in the ab -plane, as marked in red in Figure 8j–l, with a similar barrier of 0.809 eV (Figure 8l). However, the barrier of migration between adjacent layers is significantly higher (2.987 eV), as marked in blue in Figure 8k,l.

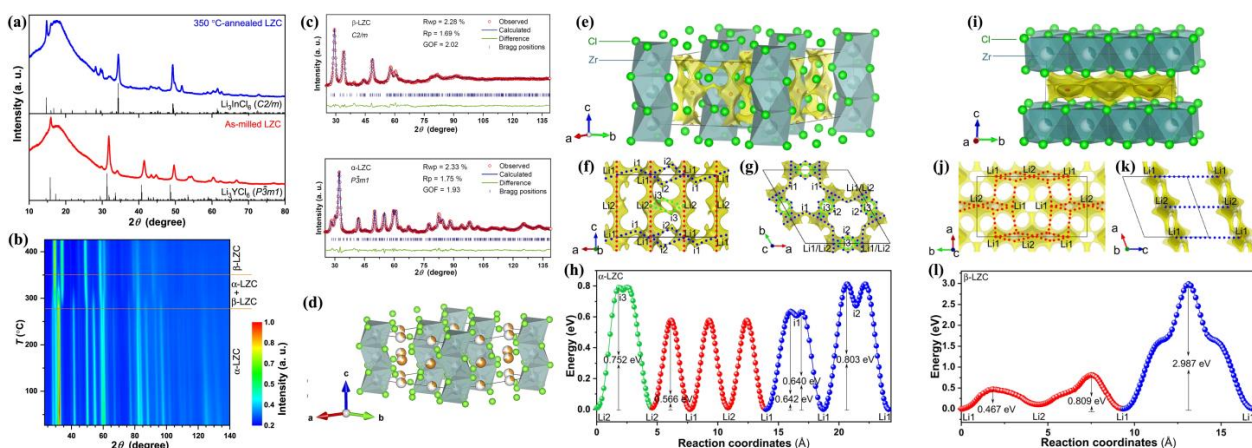


Figure 8. (a) XRD data collected for as-milled α -LZC and 350 °C-annealed β -LZC. (b) In situ NPD profile of the dependence on temperature from 27 to 427 °C for the as-milled LZC. (c) NPD Rietveld refinements for the as-milled β -LZC at 427 °C and α -LZC at 27 °C. (d) The structural model of α -LZC obtained from the NPD Rietveld refinement. The brown, bluish-grey, light-green balls represent Li, Zr, Cl atoms, respectively. (e) The crystal structures of α -LZC covered with Li⁺ potential map. (f,g) Possible Li⁺ migration pathways of α -LZC viewed along *b* and *c*-directions. (h) Extracted energy profiles corresponding to different migration pathways in α -LZC. (i) The crystal structures of β -LZC with superimposed Li ion potential map. (j,k) Possible Li⁺ migration pathways of β -LZC viewed along *c* and *b*-directions. (l) Extracted energy profiles corresponding to different migration pathways in β -LZC. Noted that each energy profile corresponds to the pathway of the same color in (h,l), respectively. Reproduced with permission: Copyright 2021, Springer Nature [68].

However, the author proposed that the true reason for the higher ionic conductivity of α -LZC should be attributed to non-periodic features including defects, surface structure, amorphous phase, etc., which are induced by the high-energy intense ball milling during synthesis. This is because, first, the effective migration barriers of α -LZC (0.803 eV) and β -LZC (0.809 eV) are similar, and second, the conductivity of as-milled α -LZC will drop to $3.22 \times 10^{-5} \text{ S cm}^{-1}$ after being annealed at 215 °C. Yet, further investigation using advanced techniques with ultrahigh spatial resolution is still required to identify the microscopic mechanism of the fast ionic transport and make a rational optimization. In spite of this, this work can be seen as a good illustration of how an in situ NPD technique provides an in-depth understanding of the structure–property relationship of advanced SSEs. Li₂ZrCl₆ SSE is cost-effective, moisture-resistant (5% relative humidity), deformable, and cathode compatible (4 V-class). Specifically, its merits of humidity tolerance and cost-effectiveness remove two major obstacles in the way towards wide usage of SSEs.

4. Perspective

Generally, we have reviewed the utilization of neutron powder diffraction (NPD) in the metal halides family. NPD as a powerful technology provides an in-depth understanding of the interplay between their structures and Li⁺ transport behavior. With its unique advantage of nuclei detection, NPD clearly determines the nuclear density distribution of Li⁺ ions, metal cations and halogen anions, which can be further analyzed by the BVSE method [36,37] to reveal Li⁺ migration pathways and energy landscapes. Some perspectives on future directions of NPD application in metal halide systems are presented as follows:

(1) In situ or in operando NPD analysis of metal halide SSEs during battery charging/discharging process. This in situ NPD allows direct experimental observation of Li migration pathways during the charging/discharging process, which serves as the basis for more precisely understanding this migration behavior and better designing the metal halide components. In addition, the possible deterioration of the halide crystal structure under long-time cycling could be investigated via this in situ technique.

(2) In situ or in operando NPD analysis of interfacial compatibility with electrodes without disassembling the batteries. A neutron beam possesses a stronger penetrating ability to detect the interfacial heterogeneous phases during or after the running of the battery. This technique may provide direct observation of the formation and deterioration of the interface. Failure of the interface can also be analyzed in terms of chemical and structural changes.

(3) High-resolution, high-intensity and wide d -spacing-ranged NPD for the study of novel halide SSEs with a complicated structure. High-resolution and high-intensity signals indicate a precise nuclei density distribution that is very beneficial for a facile structure determination of new phases. A wide d -spacing range indicates that diffraction peaks from lattice planes with smaller interplanar spacing can be collected, which provides key information for local disorder analysis.

(4) Combination of NPD and other advanced techniques for a comprehensive investigation of microscopic structure. NPD can be jointly used with Synchrotron, PDF, EXAFS, CT imaging, etc. Synchrotron is powerful in determining heavy ions. It provides high-intensity, high-resolution X-ray diffraction peaks to confirm the metal and halogen host lattice, in which case the NPD could focus on determining the Li^+ distribution inside. PDF (pair distribution function) and also EXAFS could be utilized in combination with NPD to analyze local structures and coordination environments, particularly in nano-crystalline SSEs. The X-ray CT imaging could reveal cracks or defects in SSEs while NPD refinement could study their origin from the perspective of residual stress in the lattice. More ways for the joint usage of NPD and other characterizations are still being explored to tackle more complicated issues in SSEs.

To date, research in SSEs for ASSBs have made a giant leap in the past decades, with a variety of different SSEs being discovered. However, a series of thorny problems still stand in the way towards advancing SSEs for next generation ASSBs, including ionic conductivity, electrochemical stability, and large-scale fabrication. Addressing the above problems robustly requires support from neutron powder diffraction to yield fundamental and structural understanding for the delicate design of advanced SSEs. It can be anticipated that more powerful NPD technology will emerge in the near future to assist SSEs development, and NPD will as always play an indispensable role in this research.

Author Contributions: Conceptualization, H.Z. and W.X.; writing—original draft preparation, H.Z., F.X. and X.C.; writing—review and editing, H.Z., W.X., F.X. and X.C.; supervision, H.Z. All authors have read and agreed to the published version of the manuscript.

Funding: This review is funded by the National Natural Science Foundation of China (52103333).

Data Availability Statement: We agree to share all data. All data and high-resolution figures are available on the MDPI battery journal.

Conflicts of Interest: The authors declare no conflict of interest. The funders had no role in the writing of the manuscript.

References

1. Trahey, L.; Brushett, F.R.; Balsara, N.P.; Ceder, G.; Cheng, L.; Chiang, Y.M.; Hahn, N.T.; Ingram, B.J.; Minter, S.D.; Moore, J.S.; et al. Energy storage emerging: A perspective from the Joint Center for Energy Storage Research. *Proc. Natl. Acad. Sci. USA* **2020**, *117*, 12550–12557. [[CrossRef](#)] [[PubMed](#)]
2. Lee, Y.G.; Fujiki, S.; Jung, C.; Suzuki, N.; Yashiro, N.; Omoda, R.; Ko, D.S.; Shiratsuchi, T.; Sugimoto, T.; Ryu, S.; et al. High-energy long-cycling all-solid-state lithium metal batteries enabled by silver–carbon composite anodes. *Nat. Energy* **2020**, *5*, 299–308. [[CrossRef](#)]
3. Randau, S.; Weber, D.A.; Kotz, O.; Koerver, R.; Braun, P.; Weber, A.; Ivers-Tiffée, E.; Adermann, T.; Kulisch, J.; Zeier, W.G.; et al. Benchmarking the performance of all-solid-state lithium batteries. *Nat. Energy* **2020**, *5*, 259–270. [[CrossRef](#)]
4. Bachman, J.C.; Mui, S.; Grimaud, A.; Chang, H.H.; Pour, N.; Lux, S.F.; Paschos, O.; Maglia, F.; Lupart, S.; Lamp, P.; et al. Inorganic Solid-State Electrolytes for Lithium Batteries: Mechanisms and Properties Governing Ion Conduction. *Chem. Rev.* **2016**, *116*, 140–162. [[CrossRef](#)]
5. Zhang, Z.Z.; Shao, Y.J.; Lotsch, B.; Hu, Y.S.; Li, H.; Janek, J.; Nazar, L.F.; Nan, C.W.; Maier, J.; Armand, M.; et al. New horizons for inorganic solid state ion conductors. *Energy Environ. Sci.* **2018**, *11*, 1945–1976. [[CrossRef](#)]

6. Xia, W.; Zhao, Y.; Zhao, F.P.; Adair, K.G.; Zhao, R.; Li, S.; Zou, R.Q.; Zhao, Y.S.; Sun, X.L. Antiperovskite Electrolytes for Solid-State Batteries. *Chem. Rev.* **2022**, *122*, 3763–3819. [[CrossRef](#)]
7. Wang, J.B.; Komine, Y.; Notohara, H.; Urita, K.; Moriguchi, I.; Wei, M.D. The optimized interface engineering of VS₂ as cathodes for high performance all-solid-state lithium-ion battery. *Sci. China Technol. Sci.* **2022**, *65*, 1859–1866. [[CrossRef](#)]
8. Wang, J.B.; Huang, J.J.; Huang, S.P.; Komine, Y.; Notohara, H.; Urita, K.; Moriguchi, I.; Wei, M.D. Regulating the effects of SnS shrinkage in all-solid-state lithium-ion batteries with excellent electrochemical performance. *Chem. Eng. J.* **2022**, *429*, 132424. [[CrossRef](#)]
9. Kamaya, N.; Homma, K.; Yamakawa, Y.; Hirayama, M.; Kanno, R.; Yonemura, M.; Kamiyama, T.; Kato, Y.; Hama, S.; Kawamoto, K.; et al. A lithium superionic conductor. *Nat. Mater.* **2011**, *10*, 682–686. [[CrossRef](#)]
10. Kato, Y.; Hori, S.; Saito, T.; Suzuki, K.; Hirayama, M.; Mitsui, A.; Yonemura, M.; Iba, H.; Kanno, R. High-power all-solid-state batteries using sulfide superionic conductors. *Nat. Energy* **2016**, *1*, 1–7. [[CrossRef](#)]
11. Walther, F.; Koerver, R.; Fuchs, T.; Ohno, S.; Sann, J.; Rohnke, M.; Zeier, W.G.; Janek, J. Visualization of the Interfacial Decomposition of Composite Cathodes in Argyrodite-Based All-Solid-State Batteries Using Time-of-Flight Secondary-Ion Mass Spectrometry. *Chem. Mater.* **2019**, *31*, 3745–3755. [[CrossRef](#)]
12. Schwietert, T.K.; Arszewska, V.A.; Wang, C.; Yu, C.; Vasileiadis, A.; de Klerk, N.J.J.; Hageman, J.; Hupfer, T.; Kerkamm, I.; Xu, Y.L.; et al. Clarifying the relationship between redox activity and electrochemical stability in solid electrolytes. *Nat. Mater.* **2020**, *19*, 428. [[CrossRef](#)] [[PubMed](#)]
13. Dewald, G.F.; Ohno, S.; Kraft, M.A.; Koerver, R.; Till, P.; Vargas-Barbosa, N.M.; Janek, J.; Zeier, W.G. Experimental Assessment of the Practical Oxidative Stability of Lithium Thiophosphate Solid Electrolytes. *Chem. Mater.* **2019**, *31*, 8328–8337. [[CrossRef](#)]
14. Liang, J.W.; Li, X.N.; Adair, K.R.; Sun, X.L. Metal Halide Superionic Conductors for All-Solid-State Batteries. *Acc. Chem. Res.* **2021**, *54*, 1023–1033. [[CrossRef](#)]
15. Banerjee, A.; Wang, X.F.; Fang, C.C.; Wu, E.A.; Meng, Y.S. Interfaces and Interphases in All-Solid-State Batteries with Inorganic Solid Electrolytes. *Chem. Rev.* **2020**, *120*, 6878–6933. [[CrossRef](#)]
16. Wang, S.; Bai, Q.; Nolan, A.M.; Liu, Y.S.; Gong, S.; Sun, Q.; Mo, Y.F. Lithium Chlorides and Bromides as Promising Solid-State Chemistries for Fast Ion Conductors with Good Electrochemical Stability. *Angew. Chem. Int. Ed.* **2019**, *58*, 8039–8043. [[CrossRef](#)]
17. Li, X.N.; Liang, J.W.; Yang, X.F.; Adair, K.R.; Wang, C.H.; Zhao, F.P.; Sun, X.L. Progress and perspectives on halide lithium conductors for all-solid-state lithium batteries. *Energy Environ. Sci.* **2020**, *13*, 1429–1461. [[CrossRef](#)]
18. Plichta, E.J.; Behl, W.K.; Vujic, D.; Chang, W.H.S.; Schleich, D.M. The Rechargeable Li_xTiS₂/LiAlCl₄/Li_{1-x}CoO₂ Solid-State Cell. *J. Electrochem. Soc.* **1992**, *139*, 1509–1513. [[CrossRef](#)]
19. Spector, J.; Villeneuve, G.; Hanebali, L.; Cros, C. NMR Investigations of the Li⁺ ion mobility in the double chlorides Li₂MgCl₄ and LiMgCl₃. *Mater. Lett.* **1982**, *1*, 43–48. [[CrossRef](#)]
20. Weppner, W.; Huggins, R.A. Thermodynamic and phase equilibrium studies of the fast solid ionic conductor LiAlCl₄. *Solid State Ionics* **1980**, *1*, 3–14. [[CrossRef](#)]
21. Asano, T.; Sakai, A.; Ouchi, S.; Sakaida, M.; Miyazaki, A.; Hasegawa, S. Solid Halide Electrolytes with High Lithium-Ion Conductivity for Application in 4 V Class Bulk-Type All-Solid-State Batteries. *Adv. Mater.* **2018**, *30*, e1803075. [[CrossRef](#)] [[PubMed](#)]
22. Li, X.N.; Liang, J.W.; Luo, J.; Banis, M.N.; Wang, C.H.; Li, W.H.; Deng, S.X.; Yu, C.; Zhao, F.P.; Hu, Y.F.; et al. Air-stable Li₃InCl₆ electrolyte with high voltage compatibility for all-solid-state batteries. *Energy Environ. Sci.* **2019**, *12*, 2665–2671. [[CrossRef](#)]
23. Li, X.N.; Liang, J.W.; Chen, N.; Luo, J.; Adair, K.R.; Wang, C.H.; Banis, M.N.; Sham, T.K.; Zhang, L.; Zhao, S.Q.; et al. Water-Mediated Synthesis of a Superionic Halide Solid Electrolyte. *Angew. Chem. Int. Ed.* **2019**, *58*, 16427–16432. [[CrossRef](#)] [[PubMed](#)]
24. Park, K.H.; Kaup, K.; Assoud, A.; Zhang, Q.; Wu, X.H.; Nazar, L.F. High-Voltage Superionic Halide Solid Electrolytes for All-Solid-State Li-Ion Batteries. *ACS Energy Lett.* **2020**, *5*, 533–539. [[CrossRef](#)]
25. Kim, S.Y.; Kaup, K.; Park, K.H.; Assoud, A.; Zhou, L.D.; Liu, J.; Wu, X.H.; Nazar, L.F. Lithium Ytterbium-Based Halide Solid Electrolytes for High Voltage All-Solid-State Batteries. *ACS Mater. Lett.* **2021**, *3*, 930–938. [[CrossRef](#)]
26. Liang, J.W.; Li, X.N.; Wang, S.; Adair, K.R.; Li, W.H.; Zhao, Y.; Wang, C.H.; Hu, Y.F.; Zhang, L.; Zhao, S.Q.; et al. Site-Occupation-Tuned Superionic Li(x)ScCl(3+x)Halide Solid Electrolytes for All-Solid-State Batteries. *J. Am. Chem. Soc.* **2020**, *142*, 7012–7022. [[CrossRef](#)] [[PubMed](#)]
27. Kwak, H.; Han, D.; Lyoo, J.; Park, J.; Jung, S.H.; Han, Y.; Kwon, G.; Kim, H.; Hong, S.T.; Nam, K.W.; et al. New Cost-Effective Halide Solid Electrolytes for All-Solid-State Batteries: Mechanochemically Prepared Fe³⁺-Substituted Li₂ZrCl₆. *Adv. Energy Mater.* **2021**, *11*, 2003190. [[CrossRef](#)]
28. Park, J.; Han, D.; Kwak, H.; Han, Y.; Choi, Y.J.; Nam, K.W.; Jung, Y.S. Heat treatment protocol for modulating ionic conductivity via structural evolution of Li_{3-x}Yb_{1-x}M_xCl₆ (M = Hf⁴⁺, Zr⁴⁺) new halide superionic conductors for all-solid-state batteries. *Chem. Eng. J.* **2021**, *425*, 130630. [[CrossRef](#)]
29. Zhou, L.D.; Kwok, C.Y.; Shyamsunder, A.; Zhang, Q.; Wu, X.H.; Nazar, L.F. A new halospinel superionic conductor for high-voltage all solid state lithium batteries. *Energy Environ. Sci.* **2020**, *13*, 2056–2063. [[CrossRef](#)]
30. Li, X.N.; Liang, J.W.; Adair, K.R.; Li, J.J.; Li, W.H.; Zhao, F.P.; Hu, Y.F.; Sham, T.K.; Zhang, L.; Zhao, S.Q.; et al. Origin of Superionic Li₃Y_{1-x}In_xCl₆ Halide Solid Electrolytes with High Humidity Tolerance. *Nano Lett.* **2020**, *20*, 4384–4392. [[CrossRef](#)]
31. Feinauer, M.; Euchner, H.; Fichtner, M.; Reddy, M.A. Unlocking the Potential of Fluoride-Based Solid Electrolytes for Solid-State Lithium Batteries. *ACS Appl. Energy Mater.* **2019**, *2*, 7196–7203. [[CrossRef](#)]

32. Bacon, G.E. *Neutron Diffraction*, 3rd ed.; Clarendon Pr.: Oxford, UK, 1975.
33. Shannon, R.D. Revised Effective Ionic Radii and Systematic Studies of Interatomic Distances in Halides and Chalcogenides. *Acta Cryst.* **1976**, *32*, 751–767. [[CrossRef](#)]
34. Petricek, V.; Dusek, M.; Palatinus, L. Crystallographic Computing System JANA2006: General features. *Z. Krist. Cryst. Mater.* **2014**, *229*, 345–352. [[CrossRef](#)]
35. Rodriguez-Carvajal, J. Recent Advances in Magnetic Structure Determination by Neutron Powder Diffraction. *Phys. B* **1993**, *192*, 55–69. [[CrossRef](#)]
36. Chen, H.M.; Wong, L.L.; Adams, S. SoftBV—A software tool for screening the materials genome of inorganic fast ion conductors. *Acta Crystallogr. Sect. B Struct. Sci. Cryst. Eng. Mater.* **2019**, *75*, 18–33. [[CrossRef](#)]
37. Wong, L.L.; Phuah, K.C.; Dai, R.Y.; Chen, H.M.; Chew, W.S.; Adams, S. Bond Valence Pathway Analyzer—An Automatic Rapid Screening Tool for Fast Ion Conductors within softBV. *Chem. Mater.* **2021**, *33*, 625–641. [[CrossRef](#)]
38. Gao, L.; Zhang, H.; Wang, Y.C.; Li, S.; Zhao, R.; Wang, Y.G.; Gao, S.; He, L.H.; Song, H.F.; Zou, R.Q.; et al. Mechanism of enhanced ionic conductivity by rotational nitrite group in antiperovskite Na₃ONO₂. *J. Mater. Chem. A* **2020**, *8*, 21265–21272. [[CrossRef](#)]
39. Van der Ven, A.; Bhattacharya, J.; Belak, A.A. Understanding Li Diffusion in Li-Intercalation Compounds. *Acc. Chem. Res.* **2013**, *46*, 1216–1225. [[CrossRef](#)]
40. Helm, B.; Schlem, R.; Wankmiller, B.; Banik, A.; Gautam, A.; Ruhl, J.; Li, C.; Hansen, M.R.; Zeier, W.G. Exploring Aliovalent Substitutions in the Lithium Halide Superionic Conductor Li_{3-x}In_{1-x}Zr_xCl₆ (0 ≤ x ≤ 0.5). *Chem. Mater.* **2021**, *33*, 4773–4782.
41. Zhou, L.D.; Zuo, T.T.; Li, C.; Zhang, Q.; Janek, J.; Nazar, L.F. Li_{3-x}Zr_x(Ho/Lu)_(1-x)Cl₆ Solid Electrolytes Enable Ultrahigh-Loading Solid-State Batteries with a Prelithiated Si Anode. *ACS Energy Lett.* **2023**, *8*, 3102–3111. [[CrossRef](#)]
42. Liang, J.W.; van der Maas, E.; Luo, J.; Li, X.N.; Chen, N.; Adair, K.R.; Li, W.H.; Li, J.J.; Hu, Y.F.; Liu, J.; et al. A Series of Ternary Metal Chloride Superionic Conductors for High-Performance All-Solid-State Lithium Batteries. *Adv. Energy Mater.* **2022**, *12*, 2103921. [[CrossRef](#)]
43. Bohnsack, A.; Stenzel, F.; Zajonc, A.; Balzer, G.; Wickleder, M.S.; Meyer, G. Ternäre Chloride der Selten-Erd-Elemente mit Lithium, Li₃MC₁₆ (M = Tb–Lu, Y, Sc): Synthese, Kristallstrukturen und Ionenbewegung. *Z. Anorg. Allg. Chem.* **1997**, *623*, 1067–1073. [[CrossRef](#)]
44. Sacci, R.L.; Bennett, T.H.; Drews, A.R.; Anandan, V.; Kirkham, M.J.; Daemen, L.L.; Nanda, J. Phase evolution during lithium-indium halide superionic conductor dehydration. *J. Mater. Chem. A* **2021**, *9*, 990–996. [[CrossRef](#)]
45. Yamamoto, R.K.Y.T.O. Structure, Ionic Conductivity and Phase Transformation of Double Chloride Spinel. *Solid State Ion.* **1988**, *28*, 1276–1281.
46. Lutz, H.D.; Schmidt, W.; Haeuselner, H. Chloride Spinel: A New Group of Solid Lithium Electrolytes. *J. Phys. Chem. Solids* **1981**, *42*, 287–289. [[CrossRef](#)]
47. Zhou, L.D.; Assoud, A.; Zhang, Q.; Wu, X.H.; Nazar, L.F. New Family of Argyrodite Thioantimonate Lithium Superionic Conductors. *J. Am. Chem. Soc.* **2019**, *141*, 19002–19013. [[CrossRef](#)]
48. Zhou, L.D.; Assoud, A.; Shyamsunder, A.; Huq, A.; Zhang, Q.; Hartmann, P.; Kulisch, J.; Nazar, L.F. An Entropically Stabilized Fast-Ion Conductor: Li_{3-3.25}[Si_{1.25}P_{0.75}]S₄. *Chem. Mater.* **2019**, *31*, 7801–7811. [[CrossRef](#)]
49. Canepa, P.; Bo, S.H.; Gautam, G.S.; Key, B.; Richards, W.D.; Shi, T.; Tian, Y.S.; Wang, Y.; Li, J.C.; Ceder, G. High magnesium mobility in ternary spinel chalcogenides. *Nat. Commun.* **2017**, *8*, 1759. [[CrossRef](#)]
50. Zhou, L.D.; Zuo, T.T.; Kwok, C.Y.; Kim, S.Y.; Assoud, A.; Zhang, Q.; Janek, J.; Nazar, L.F. High areal capacity, long cycle life 4 V ceramic all-solid-state Li-ion batteries enabled by chloride solid electrolytes. *Nat. Energy* **2022**, *7*, 83–93. [[CrossRef](#)]
51. Rice, M.R.W. Ionic transport in super ionic conductors: A theoretical model. *J. Solid State Chem.* **1972**, *4*, 294–310. [[CrossRef](#)]
52. Wakamura, K. Roles of phonon amplitude and low-energy optical phonons on superionic conduction. *Phys. Rev. B* **1997**, *56*, 11593–11599. [[CrossRef](#)]
53. Yu, C.; Li, Y.; Adair, K.R.; Li, W.H.; Goubitz, K.; Zhao, Y.; Willans, M.J.; Thijs, M.A.; Wang, C.H.; Zhao, F.P.; et al. Tuning ionic conductivity and electrode compatibility of Li₃YBr₆ for high-performance all solid-state Li batteries. *Nano Energy* **2020**, *77*, 105097. [[CrossRef](#)]
54. Schlem, R.; Berges, T.; Li, C.; Kraft, M.A.; Minafra, N.; Zeier, W.G. Lattice Dynamical Approach for Finding the Lithium Superionic Conductor Li₃ErI₆. *ACS Appl. Energy Mater.* **2020**, *3*, 3684–3691. [[CrossRef](#)]
55. Liu, Z.T.; Ma, S.; Liu, J.; Xiong, S.; Ma, Y.F.; Chen, H.L. High Ionic Conductivity Achieved in Li₃Y(Br₃Cl₃) Mixed Halide Solid Electrolyte via Promoted Diffusion Pathways and Enhanced Grain Boundary. *ACS Energy Lett.* **2020**, *6*, 298–304. [[CrossRef](#)]
56. Jiang, M.; Key, B.; Meng, Y.S.; Grey, C.P. Electrochemical and Structural Study of the Layered, “Li-Excess” Lithium-Ion Battery Electrode Material Li₁₁/9Ni₁/3Mn₅/9 O₂. *Chem. Mater.* **2009**, *21*, 2733–2745. [[CrossRef](#)]
57. Ma, J.; Bo, S.H.; Wu, L.J.; Zhu, Y.M.; Grey, C.P.; Khalifah, P.G. Ordered and Disordered Polymorphs of Na(Ni₂/3Sb₁/3)O₂: Honeycomb-Ordered Cathodes for Na-Ion Batteries. *Chem. Mater.* **2015**, *27*, 2387–2399. [[CrossRef](#)]
58. van der Maas, E.; Zhao, W.; Cheng, Z.; Famprikis, T.; Thijs, M.; Parnell, S.R.; Ganapathy, S.; Wagemaker, M. Investigation of Structure, Ionic Conductivity, and Electrochemical Stability of Halogen Substitution in Solid-State Ion Conductor Li₃YBr_xCl_{6-x}. *J. Phys. Chem. C* **2022**, *127*, 125–132. [[CrossRef](#)] [[PubMed](#)]
59. Culver, S.P.; Koerver, R.; Krauskopf, T.; Zeier, W.G. Designing Ionic Conductors: The Interplay between Structural Phenomena and Interfaces in Thiophosphate-Based Solid-State Batteries. *Chem. Mater.* **2018**, *30*, 4179–4192. [[CrossRef](#)]
60. Tang, W.; Xia, W.; Hussain, F.; Zhu, J.L.; Han, S.B.; Yin, W.; Yu, P.C.; Lei, J.W.; Butenko, D.S.; Wang, L.P.; et al. A dual-halogen electrolyte for protective-layer-free all-solid-state lithium batteries. *J. Power Sources* **2023**, *568*, 232992. [[CrossRef](#)]

61. Yu, T.W.; Liang, J.W.; Luo, L.; Wang, L.M.; Zhao, F.P.; Xu, G.F.; Bai, X.T.; Yang, R.; Zhao, S.Q.; Wang, J.T.; et al. Superionic Fluorinated Halide Solid Electrolytes for Highly Stable Li-Metal in All-Solid-State Li Batteries. *Adv. Energy Mater.* **2021**, *11*, 2101915. [[CrossRef](#)]
62. Chen, X.; Jia, Z.Q.; Lv, H.M.; Wang, C.G.; Zhao, N.; Guo, X.X. Improved stability against moisture and lithium metal by doping F into Li₃InCl₆. *J. Power Sources* **2022**, *545*, 231939. [[CrossRef](#)]
63. Yin, Y.C.; Yang, J.T.; Luo, J.D.; Lu, G.X.; Huang, Z.Y.; Wang, J.P.; Li, P.; Li, F.; Wu, Y.C.; Tian, T.; et al. A LaCl₃-based lithium superionic conductor compatible with lithium metal. *Nature* **2023**, *616*, 77–83. [[CrossRef](#)] [[PubMed](#)]
64. He, X.F.; Bai, Q.; Liu, Y.S.; Nolan, A.M.; Ling, C.; Mo, Y.F. Crystal Structural Framework of Lithium Super-Ionic Conductors. *Adv. Energy Mater.* **2019**, *9*, 1902078. [[CrossRef](#)]
65. Brugge, R.H.; Hekselman, A.K.O.; Cavallaro, A.; Pesci, F.M.; Chater, R.J.; Kilner, J.A.; Agüadero, A. Garnet Electrolytes for Solid State Batteries: Visualization of Moisture-Induced Chemical Degradation and Revealing Its Impact on the Li-Ion Dynamics. *Chem. Mater.* **2018**, *30*, 3704–3713. [[CrossRef](#)]
66. Zhu, Y.Z.; Mo, Y.F. Materials Design Principles for Air-Stable Lithium/Sodium Solid Electrolytes. *Angew. Chem. Int. Ed.* **2020**, *59*, 17472–17476. [[CrossRef](#)] [[PubMed](#)]
67. Hayashi, A.; Muramatsu, H.; Ohtomo, T.; Hama, S.; Tatsumisago, M. Improvement of chemical stability of Li₃PS₄ glass electrolytes by adding MxO_y (M = Fe, Zn, and Bi) nanoparticles. *J. Mater. Chem. A* **2013**, *1*, 6320–6326. [[CrossRef](#)]
68. Wang, K.; Ren, Q.Y.; Gu, Z.Q.; Duan, C.M.; Wang, J.Z.; Zhu, F.; Fu, Y.Y.; Hao, J.P.; Zhu, J.F.; He, L.H.; et al. A cost-effective and humidity-tolerant chloride solid electrolyte for lithium batteries. *Nat. Commun.* **2021**, *12*, 4410. [[CrossRef](#)]

Disclaimer/Publisher’s Note: The statements, opinions and data contained in all publications are solely those of the individual author(s) and contributor(s) and not of MDPI and/or the editor(s). MDPI and/or the editor(s) disclaim responsibility for any injury to people or property resulting from any ideas, methods, instructions or products referred to in the content.